

High-Pressure Argon gas TPC Option for the DUNE Near Detector

DUNE HPgTPC WG

Fermi National Accelerator Laboratory, Box 500, Batavia, IL 60510-5011, USA

ABSTRACT: The high-pressure Ar gas TPC (HPgTPC) Option for the DUNE Near Detector is a fine-grained tracker with an active volume approximately 5 m in diameter by 5 m long. This cylindrical geometry is a copy of the ALICE TPC and it is assumed that we will re-purpose the ALICE readout chambers, which will become available in 2019. Two new readout chambers will have to be built, however, to fill the central barrel region. Assuming 10 Atm operation, the total active mass of the detector is ≈ 1.8 t with a fiducial mass of ≈ 1 t. This fiducial mass produces $\approx 1.6 \times 10^6$ CC ν_μ events per year of exposure. In this report, we will describe how this fine-grained tracker functions as part of the near detector suite of instrumentation and will answer specific questions raised by the ND conveners.

Contents

1	Executive Summary	2
2	Overview	3
3	Analysis Magnet	3
3.1	HPgTPC inside dipole magnet	3
3.1.1	Basic configuration and event statistics	3
3.2	HPgTPC inside KLOE magnet	5
4	Details of HPgTPC performance inside the dipole magnet	5
4.1	Tracking efficiency	6
4.2	Particle Identification	6
4.3	Charged particle detection thresholds	7
4.3.1	MARS study of particle detection thresholds	7
4.4	Momentum and angular resolution for charged particles	10
4.4.1	Electrons	10
4.5	ECAL design and performance	12
4.5.1	Overall ECAL design	12
4.5.2	Active elements of ECAL	13
4.5.3	Simulated ECAL performance	14
4.6	Neutron detection capabilities	17
4.6.1	Discussion	17
4.7	Performance for key channels	22
4.7.1	Energy Resolution of ν_μ CC Events as a Function of Detection Threshold	22
4.7.2	Distinguishing among nuclear models in neutrino interaction generators	23
4.7.3	CC and NC Coherent Pion Production	23
4.7.4	Low- ν Events	25
4.7.5	Background to ν_e Charged Current Interactions	25
4.8	Full pattern recognition and reconstruction utilizing ALICE code framework	26
5	Performance of integrated Ar detector, iArDet: ArgonCube + HPgTPC	26
5.1	Cross section measurements on argon in a magnetized detector	26
5.2	Intrinsic ν_e rate measurement and constraining backgrounds to LArTPC interactions	26
5.3	HPgTPC acceptance for muons originating in ArgonCube	27
6	Conclusions	29
A	Towards a fully integrated Argon detector design	30
A.1	Thin-wall cryostat for ArgonCube	30
A.1.1	Introduction	30
A.1.2	Membrane Cryostat Background Information	30

A.1.3	35-ton Experiment- Summary of Successfully Built Membrane Cryostat	30
A.1.4	Design Proposal for ArgonCube Cryostat	31
A.1.5	FEA Results of G10 Window in ArgonCube Cryostat	34
A.1.6	Analysis with Carbon-fiber window for the ArgonCube Cryostat	36
A.1.7	Conclusions	36
A.2	Dipole magnet considerations	38
A.3	TPC Pressure vessel design	41
B	HP TPC test Stand	41
B.1	Test vessel	42
B.2	Readout chamber and field cage	42
B.3	Readout electronics and DAQ system	43
B.4	Gas system	44
B.5	Near-future schedule for the test stand	45

1 Executive Summary

This report describes the current status of the design and performance of the high-pressure gas TPC (HPgTPC) option for the magnetized multi-purpose tracker, which is one component of the DUNE near detector system. The preferred solution employs a TPC that will be a “copy” of the ALICE TPC, in that we would plan to use the ALICE readout chambers in the same geometry that they are currently used in the ALICE experiment. They will become available in 2019. Two additional chambers that are approximately 1.6 m in diameter will have to be constructed in order to fill in the central tracking region of ALICE, which employs silicon detectors. The DUNE HPgTPC will be a single gas volume that is ≈ 5.2 m in diameter and 5 m long (2.5 m + 2.5 m drift). This implementation would require a new dipole magnet of similar design and same magnetic volume as the one that is outlined in the DUNE near detector CDR, but would require a different aspect ratio. We have also performed a preliminary evaluation of the dipole design that incorporates superconducting coils and a cylindrical geometry that matches that of the HPgTPC. This is described in Appendix A. In the case where DUNE chooses to use the KLOE magnet, the size of the HPgTPC would be reduced by $\approx 61\%$ and, although some of the ALICE readout chambers could still be used, a very different geometrical arrangement would have to be incorporated. The baseline gas is the conventional TPC gas of Ar-CH₄ in a mixture ratio of 90% to 10%, the so-called P10 gas. With this mixture, 97% of the neutrino events will be on Ar nuclei, making comparisons/extrapolations to the LAr component of the near detector (ArgonCube) and the Far detector straightforward in that the nuclear effects will be the same in the three event samples. Based on extensive data on the ALICE TPC performance and utilizing performance data from PEP4, we have tabulated the expected performance of the HPgTPC with the use of these performance data and some analytical calculations. These are given in Table 1. Utilizing the dipole configuration and operating at 10 Atm, the HPgTPC will present

Table 1: HPgTPC performance.

Parameter	Value	units
σ_x	250	μm
σ_y	250	μm
σ_z	1500	μm
$\sigma_{r\phi}$	<1000	μm
Two-track separation	1	cm
Angular resolution	2-4	mrad
$\sigma(dE/dx)$	5	%
σ_{p_T}/p_T	0.7	% (10-1 GeV/c)
σ_{p_T}/p_T	1-2	% (1-0.1 GeV/c)
Energy scale uncertainty	≈ 1	% (dominated by δ_p/p)
Charge particle detection thresh.	5	MeV (K.E.)
ECAL resolution	$5-7/\sqrt{E/\text{GeV}}$	%
ECAL pointing resolution	≈ 6 at 500 MeV	degree

an active mass of $\approx 1.8\text{t}$ and a fiducial mass of $\approx 1.0\text{t}$. Using GENIE 12.2 cross-sections and the LBNF flux: 2016 CP_run15_12388 (80 GeV), $\approx 1.6 \times 10^6$ ν_μ CC events will be produced in one

year of running. Use of the KLOE magnet will reduce the number of events by the same percentage mentioned above – 61%. The first pass at an optimization of an ECAL for the HPgTPC has been done. This configuration has part of the calorimeter inside the pressure vessel for the HPgTPC and part outside. Further optimization of both the pressure vessel design and reconstruction algorithm will likely lead to performance improvements, however, preliminary performance parameters are given in Table 1.

The concept of an integrated Ar detector (iArDet) has been further developed. An engineering design study achieved a factor of 10 reduction in the thickness ($3 X_0$ to $\approx 0.3X_0$) of the cryostat for ArgonCube (for a $5\text{m} \times 5\text{m}$ window in the wall facing the HPgTPC). A preliminary magnet design study looked at replacing the room temperature coils with two superconducting coils. A 0.5T field is achievable with acceptable field non-uniformities. This removes all non-active material from the magnet from between ArgonCube and the HPgTPC pressure vessel. The total amount of dead material between ArgonCube and the HPgTPC active volume in this configuration is $< 2X_0$. In addition, the outer (outside the pressure vessel) section of the ECAL, mitigates the effects due to the pressure vessel, which represents the bulk of the non-active material between ArgonCube and the HPgTPC.

2 Overview

We are following the near detector (ND) concept endorsed by the DUNE EC which establishes that “*The baseline concept consists of a non-magnetized LAr-TPC and a magnetized multi-purpose tracker.*” The magnetized multi-purpose tracker in our case is a high-pressure (10 Atm) argon gas TPC (HPgTPC) with an electromagnetic calorimeter. Both are inside a magnetic field. We will evaluate the performance of the HPgTPC: 1) As a standalone detector capable of measuring, with superior resolution, a large subset of all interactions with the goal of reaching a fiducial mass in the gas $\gtrsim 1$ t, in order to measure a sufficient number of interactions. [Note: at this time, we are assuming that the 3D scintillator tracker is not within the magnetic volume], and 2) As a detector integrated with the LAr (the Integrated Argon Detector, or iArDet) to determine how the HPgTPC can improve the performance of ArgonCube by helping to fully measure events originating in the liquid, but which are not fully contained.

3 Analysis Magnet

In this section we will begin to document the relative merits of using either a “purpose-built” dipole magnet of a size similar to that in the DUNE CDR or the pre-existing KLOE solenoid.

3.1 HPgTPC inside dipole magnet

Here we are assuming a “purpose-built” dipole magnet with the same magnet volume as that in the DUNE near detector CDR ($\approx 162 \text{ m}^3$) with a central field of between 0.4 and 0.5 T.

3.1.1 Basic configuration and event statistics

We are now working with a cylindrical TPC geometry and thus will be essentially building a copy of the ALICE TPC using their wire- and pad-based readout chambers; they will be replacing

these chambers in 2019 with new readout chambers based on GEM amplification. In ALICE, the cylindrical TPC is the main tracking detector in the central region of the detector [1]. Two readout planes sandwich a central electrode (25 μm of aluminized mylar) at high voltage that generates the drift field, which is parallel to a 0.5 T magnetic field. On each side of the electrode, primary ionization electrons drift up to 2.5 m to reach the endcaps, which are instrumented with multi-wire proportional chamber amplification regions and cathode pad planes to read out the signals. Each endcap plane is segmented azimuthally into 18 trapezoidal regions, and further, each trapezoidal region is divided radially into an inner and outer section (the so-called inner- and outer- readout chambers, IROC and OROC).

Two new circular chambers will need to be built in order to fill in the central uninstrumented region left by reusing the existing ALICE chambers. The active dimensions of the HPgTPC will be 5.2 m in diameter and 5 m long. This HPgTPC size yields an active mass of ≈ 1.8 t. The overall system diameter is 5.94 m, which includes space for the field cage, the gas insulator, the pressure vessel and the ECAL. The total length of these components is 5.8 m, which keeps the total magnetic volume \approx to that in the CDR. A schematic of this configuration is given in the left side of Figure 1. In order to predict the event yields for one year of neutrino running, we use the 2016 DUNE Flux:

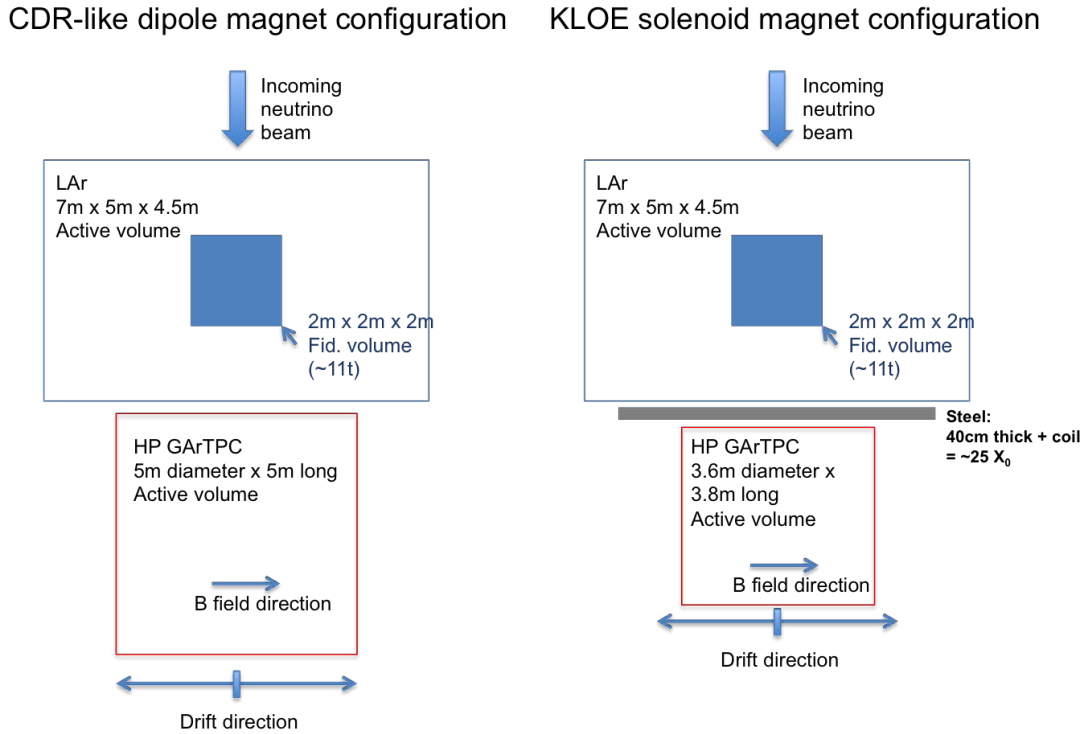


Figure 1: Configuration with CDR-like dipole magnet (left) and with existing KLOE solenoid magnet (right)

CP_run15_12388 (80 GeV), cross-sections from GENIE [2] 2.12.2 and a fiducial mass of 1 t ($\approx 55\%$ of the active mass). The gas is assumed to be 10 Atm of Ar-CH₄ mixed 90% Ar and 10% CH₄ ($\approx 97\%$ of interactions on Ar nuclei). Table 2 gives the number of events for the following interaction channels: CC total (ν_μ and ν_e), NC total (ν_μ and ν_e), CC coherent (ν_μ and ν_e), NC

coherent (ν_μ and ν_e), neutrino-electron elastic, ν_μ CC π^0 inclusive, ν_μ NC π^0 inclusive, Low- ν (250 MeV), Low- ν (100 MeV) and $\bar{\nu}_\mu$ CC coherent ($\bar{\nu}_\mu$ running).

Table 2: Number of events for 1 year of neutrino running in HP GAr TPC with 1 t fiducial mass.

Event class	Number of events per ton-year
ν_μ CC Total	1.64×10^6
ν_μ NC Total	5.17×10^5
ν_μ CC Coherent	8.35×10^3
ν_μ NC Coherent	4.8×10^3
ν_μ - electron elastic	135
ν_μ CC π^0 inclusive	4.47×10^5
ν_μ NC π^0 inclusive	1.96×10^5
ν_μ Low ν (250 MeV)	2.16×10^5
ν_μ Low ν (100 MeV)	7.93×10^4
$\bar{\nu}_\mu$ CC Coherent ($\bar{\nu}$ mode)	6.90×10^3
ν_e CC Total	1.89×10^4
ν_e NC Total	5.98×10^3
ν_e CC Coherent	93
ν_e NC Coherent	52

Based on studies done for the Near Detector Task Force, the background from interactions occurring outside the TPC is expected to be manageable: within 50 ns of an interaction in the tracker, less than 1% of simulated events had background activity in the ECAL (that is, activity that was not connected to the neutrino interaction in the tracker).

3.2 HPgTPC inside KLOE magnet

We assume a KLOE magnet design (including return iron) as described in the KLOE technical design report, with a small modification to the end iron in order to give the maximum available volume (length = magnet cryostat length) for the HPgTPC plus ECAL. Given the size of the magnet's bore and the geometry of the return yoke, we are limited to a HPgTPC with active volume approximately 3.6 m in diameter and 3.8 m long as shown in the right side of Figure 1. This yields an active mass for the HPgTPC of $\simeq 0.7$ t, significantly smaller than the mass reached with the dipole configuration.

Using the same fiducial mass to active mass ratio as was done above, we obtain a fiducial mass of 0.39 t for the largest TPC we can fit inside the pre-existing KLOE magnet. The number of events per year that we can then expect in this configuration is $\simeq 39\%$ of what is shown in Table 2.

4 Details of HPgTPC performance inside the dipole magnet

In this section we give a more detailed analysis of the performance of the HPgTPC system in the dipole magnet. The assumptions regarding the magnet are the same as the CDR (162 m³ volume and 0.4 T central field) and we assume a non-magnetized ArgonCube of dimensions 7 m \times 5 m \times 4.5 m.

4.1 Tracking efficiency

Track reconstruction in ALICE is achieved by combining hits recorded on the endcap readout pads into tracks following a trajectory that a charged particle traveled through the TPC drift volume.

The ALICE offline TPC-only track reconstruction performance is shown in Fig. 2. ALICE typically operates with particle densities ranging from 2000 to 8000 charged particles per unit rapidity (dN/dy) for central Pb-Pb interactions [3], whereas such high particle densities will never be seen with this detector placed in *any* neutrino near detector environment. The ALICE choice of

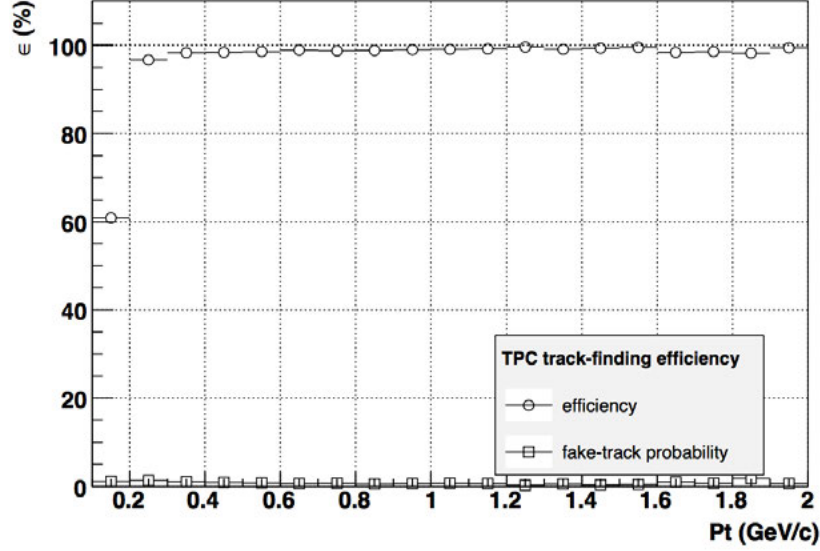


Figure 2: From Ref. [1]. Efficiency of the ALICE TPC track-finding software as a function of track transverse momentum for event multiplicity of 6000 tracks per unit of rapidity in Pb-Pb collisions (open circles), and corresponding fake track candidates (open squares).

Ne for the primary gas was driven by a number of factors, however, two-track separation capability was a primary motivation due to the extremely large event multiplicities in the experiment. Neon performs better than argon in this regard. A better comparison for the HPgTPC's operation in DUNE is the two-track separation that was obtained in PEP4 [4]. PEP4 ran an 80-20 mixture of Ar-CH₄ at 8.5 Atm. The two-track separation performance in PEP4 was 1 cm.

4.2 Particle Identification

In ALICE, the ionization produced by charged particle tracks is sampled by the TPC pad rows (there are 159 pad rows in the TPC) and a truncated mean is used for the calculation of the PID signal. Figure 3 (left) shows the ionization signals of charged particle tracks in ALICE for pp collisions at $\sqrt{s} = 7$ TeV. The different characteristic bands for various particles are clearly visible and distinct at momenta below a few GeV. If ALICE is re-purposed for the HPgTPC, we expect even better performance for particles leaving the active volume, since the detector will be operating at higher pressure (10 Atm vs. the nominal ALICE 1 Atm operation), resulting in ten times more

ionization per unit track length available for collection. Figure 3 (right) shows the charged particle identification for PEP-4/9 [5], a higher pressure gas TPC that operated at 8.5 Atm pressure.

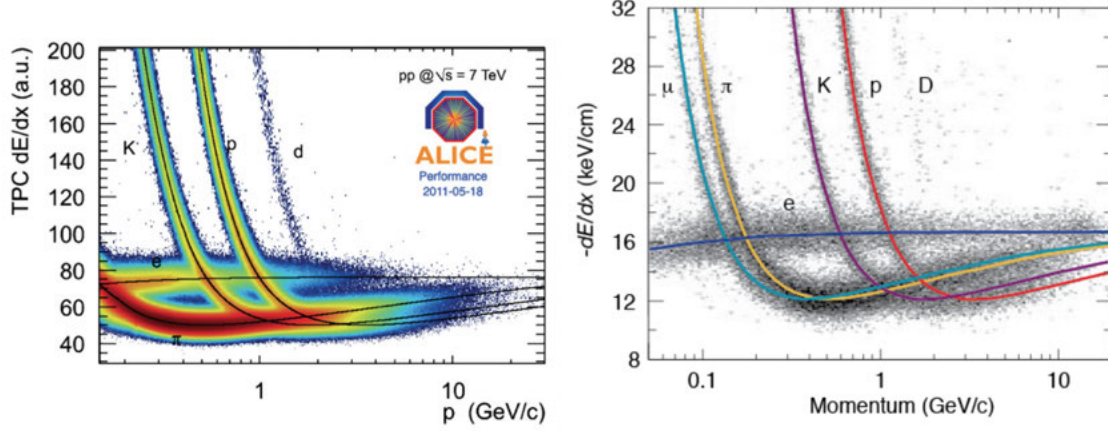


Figure 3: Left: ALICE TPC dE/dx-based particle identification as a function of momentum (from [6]). Right: PEP-4/9 TPC (80:20 Ar-CH₄, operated at 8.5 Atm) dE/dx-based particle identification.

4.3 Charged particle detection thresholds

The ability of an HPgTPC to detect lower-energy charged particles better than in a LArTPC arises from the lower-density active material, which allows particles to travel longer distances before stopping. The ranges of protons and electrons in LAr, GAr (1 Atm), and GAr (10 Atm) are shown in Figure 4. A 1 cm long stopping proton track corresponds to a kinetic energy of only 2.5 MeV in the 10 Atm HPgTPC. Very conservatively, we estimate that a 5 MeV proton (3 cm range) should be reliably detectable since it will consistently create more than two hits in the HPgTPC readout pads (the largest readout pad size in the ALICE OROC chambers is 6×15 mm. Electrons will be easily detected as well, down to even lower kinetic energies: a kinetic energy of only 0.2 MeV is required for an electron to travel 3 cm in 10 Atm argon (compared to 7 MeV required for the same range in LAr).

4.3.1 MARS study of particle detection thresholds

In addition to the analytical study that is given in the section above, a MARS simulation analysis in 10 Atm Ar-CH₄ was performed. Protons, π^- , π^+ and μ^+ with kinetic energies of 5 MeV were studied. Event displays for these four species are shown in Figure 5. The particle types are color coded as shown in Figure 6. The mean track length for these species is given in Table 3. For π^+ , π^- and μ^+ , the track length is defined as the section of the track before interaction, or at decay, obviously.

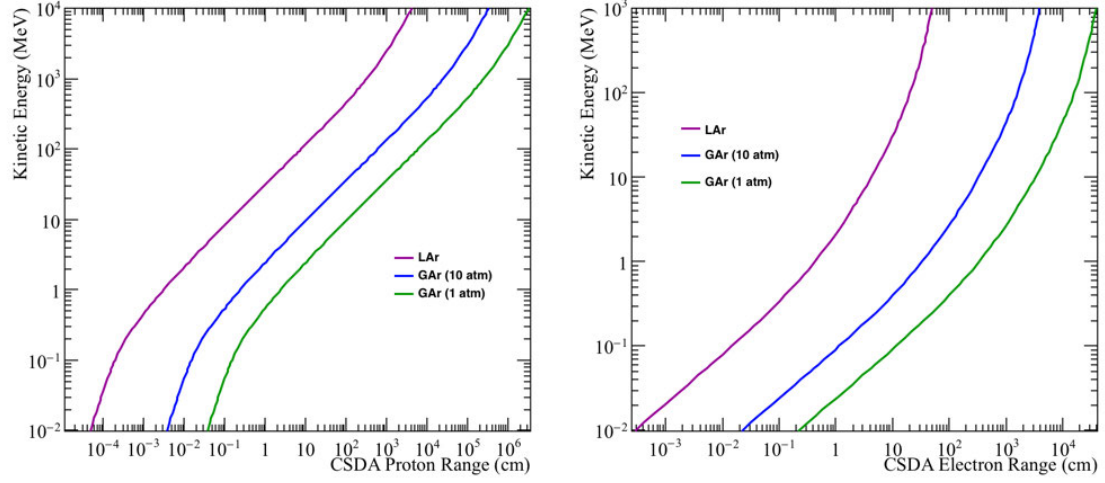
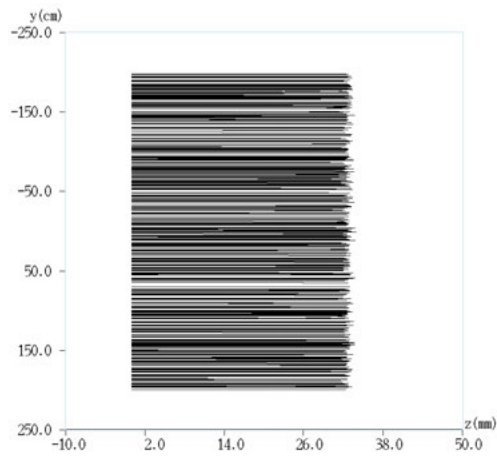


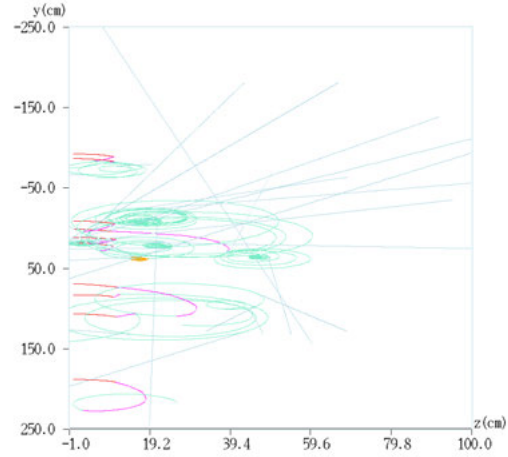
Figure 4: Ranges for protons (left) and electrons (right) to stop in liquid argon, gaseous argon (1 Atm), and gaseous argon (10 Atm), versus kinetic energy. Data are from NIST [7].

Table 3: Mean track length (cm), 5 MeV K.E..

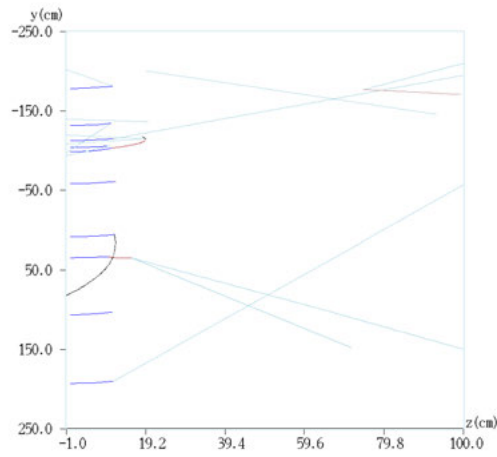
Species	Length (cm)
Protons	3
π^+	10
π^-	10
μ^+	15



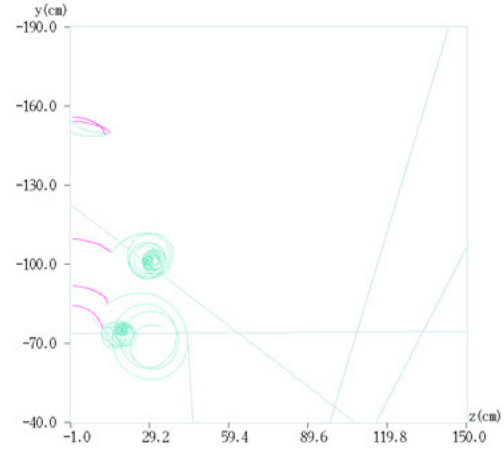
(a) 100, 5 MeV K.E. protons



(b) 5 MeV K.E. π^+



(c) 5 MeV K.E. π^-



(d) 5 MeV K.E. μ^+

Figure 5: Event displays for 5 MeV K.E. protons, π^+ , π^- and μ^+ .

Particles (1)											
ID	Name	Modify	Reset	ID	Name	Modify	Reset	ID	Name	Modify	Reset
1(on)	p			10(on)	e-			19(on)	nuam		
2(on)	n			11(on)	e+			20(on)	nue		
3(on)	pi+			12(on)	pbar			21(on)	nuae		
4(on)	pi-			13(on)	pi0			22(on)	K0		
5(on)	K+			14(on)	d			23(on)	nbar		
6(on)	K-			15(on)	t			24(on)	neu-hyp		
7(on)	mu+			16(on)	He3			25(on)	ch-hyp		
8(on)	mu-			17(on)	He4			26(on)	HI		
9(on)	gamma			18(on)	num			Reset All		Close	

Figure 6: Particle types by color.

4.4 Momentum and angular resolution for charged particles

The ability to determine the sign of a charged particle in the TPC tracking volume is limited by the spatial resolution of the measured drift points in the plane perpendicular to the magnetic field, as well as multiple Coulomb scattering (MCS) in the gas. However, for almost all tracks MCS has a small effect on momentum or angular resolution in the HPgTPC. For a fixed detector configuration, the visibility of the curvature depends on the particles p_T , the track length in the plane perpendicular to the field, and the number and closeness of nearby tracks. Because primary vertices are distributed throughout the tracking volume, the distribution of the lengths of charged-particle tracks is expected to start at very short tracks, unless sufficient fiducial volume cuts are made to ensure enough active volume remains to determine particle's track sign. Within the fiducial volume of the HPgTPC, charged-particles can be tracked over the full 4π solid angle. Even near the central electrode, tracking performance will not be degraded due to the very thin (25 μm of mylar) nature of the central electrode. The 4π coverage is true for all charged particles. ALICE ran with a central field of 0.5 T and their momentum resolution from p-Pb data [8] is shown in Figure 7.

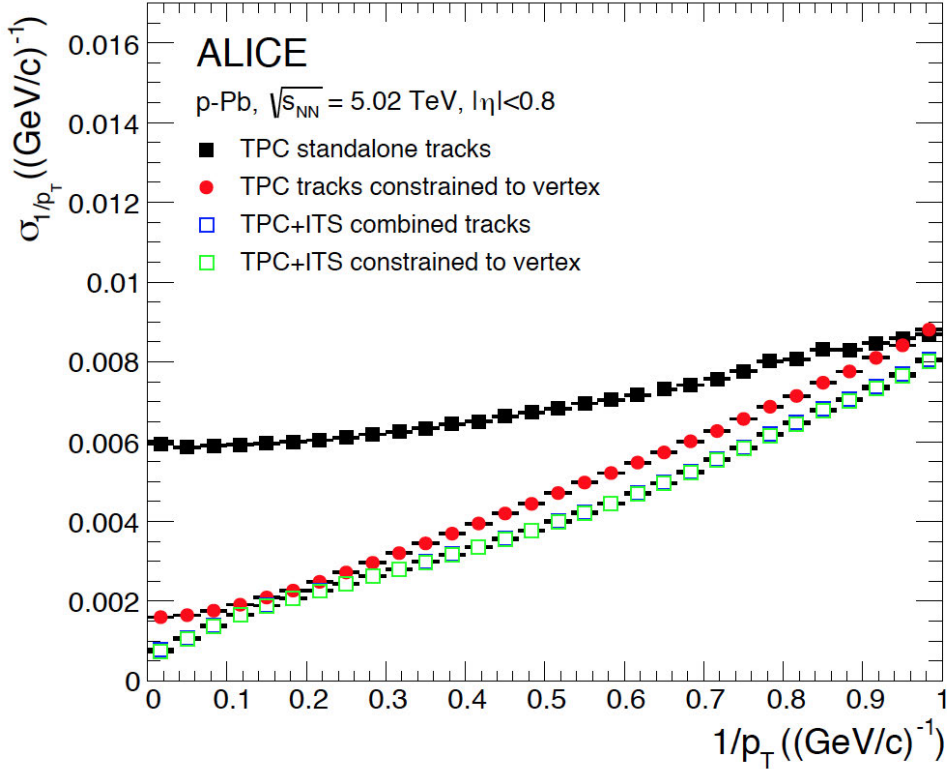


Figure 7: Black squares show the TPC stand-alone p_T resolution in ALICE for p-Pb collisions.

4.4.1 Electrons

The correct-sign fraction of electrons was studied using ν_e CC and $\bar{\nu}_e$ CC events using the unoscillated LBNF beam spectrum [9]. The GENIE [10, 11] generator was used to simulate the neutrino-nucleus interactions, and the LArSoft [12] software toolkit was used to simulate the GENIE events in gaseous

argon. One of the DUNE Far Detector geometries was used for this study, with the density of the argon in the active volume of the detector modified to be that of 10 Atm gaseous argon. In addition, a magnetic field of 0.4 T was simulated in the detector. Simulated events were required to have their primary vertices at least 30 cm away from the APAs, CPAs, and field cage walls, except for a larger requirement of 1.5 m from the downstream field cage wall, in order to remove artifacts of using the LArSoft geometry. The detector volume for the HPgTPC is much smaller than even the small Far Detector workspace geometry, and results will be shown below as functions of the track length.

In order to predict whether the sign of an electron can be measured, the sagitta of the track is computed from the GEANT4 steps. LArSoft voxelizes the active volume into cubes $300\ \mu\text{m}$ on a side, ensuring adequate coverage of tracks even when they do not interact. The procedure for computing the sagitta is to step along the electron track from the primary vertex, and for each step, examine all GEANT4 steps between the primary vertex and that step. The sagitta then is computed as the perpendicular distance between the intermediate step and the line connecting the primary vertex and the initial step, projected in the YZ plane, where the magnetic field points along the X axis. The endpoint is stepped until a sagitta sufficiently large to determine the sign is found, or until the maximum track length assumed for the detector is reached. The reason to step along the track in this manner, computing the sagitta for the growing track segment, is to reduce sensitivity to looping tracks and to multiple scattering.

Electron track steps are “cheated”, in that the primary vertex is taken from the Monte Carlo truth, electron ID is assumed to have 100% efficiency and 100% purity, and the ability to associate hits (GEANT4 steps) to the track is perfect. Some realism is injected in this study by rejecting steps on electron tracks that are within 5 mm of any other track’s steps. Steps that are within $100\ \mu\text{m}$ of a step on the electron’s track are not used to veto a step as GEANT4 simulates many very short delta rays which do not make it far enough to be detected, even in a 10 Atm gas TPC.

To simulate containment effects, only GEANT4 steps within a fixed distance of the primary vertex are considered. Two distance cuts of 1 m around the primary vertex are applied – one in the YZ plane, and the other in X. Figure 8 shows the expected performance of this method to sign electrons, assuming a minimum sagitta of 1 mm. The left-hand side of figure 8 shows correct-sign events, incorrect-sign events (of which there are none in this study), and events in which a large enough sagitta could not be found (“missing” events), as functions of the electron p_T . The right panel in Figure 8 shows the average over many tracks of the minimum distance in the YZ projection from the primary vertex to the test step needed to get a sagitta big enough (1 mm) to determine the sign.

The 1 mm minimum-sagitta cut is motivated by the space-point resolution of ALICE [6]. While the average pad size is larger ($5 \times 7\ \text{mm}$), the resolution of a space point is much better due to the charge-weighted average from clusters of hits, as well as the averaging from a Kalman-filter track fit. Neither of these techniques was applied for this study, as it assumes a perfect detector; the minimum sagitta requirement is a proxy for the reconstruction uncertainties.

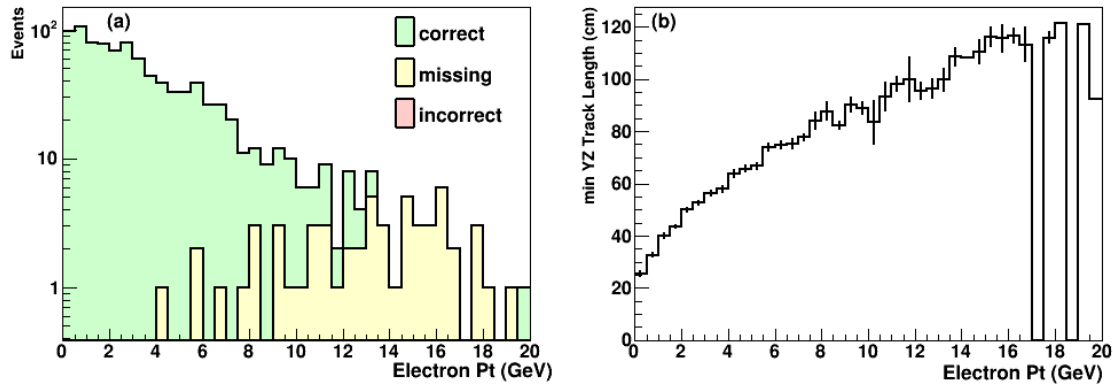


Figure 8: Left: Distribution of electron p_T for correctly-signed electrons and electrons for which the track sagitta is above 1 mm, looking only at the first 1 m of electron tracks in the YZ projection and also in X. No electron tracks were assigned the incorrect sign. Right: Average over many tracks of the minimum track length in the YZ projection needed in order to achieve a sagitta of 1 mm.

4.5 ECAL design and performance

For the electromagnetic calorimeter, a highly granular detector inspired by the design of the CALICE analog hadron calorimeter [13] is being studied. It uses plastic scintillators read out by silicon photomultipliers as active elements, sandwiched between lead absorber sheets. Since the space inside of the pressure vessel of the HPGTPC is limited, it is assumed that the calorimeter will consist of two segments, one inside and one outside of the pressure vessel. In the following, a first conceptual detector design is presented, including performance estimates based on simplified detector simulations.

4.5.1 Overall ECAL design

The design of the calorimeter is driven by two factors: Limited space inside of the pressure vessel, and the requirement for good directional resolution for the photons. The former leads to a two-segment design, one inside and one outside of the pressure vessel. The latter results in a preference for high granularity, and a high sampling frequency of the calorimeter. The two segments of the detector do not necessarily have to have the same sampling structure or granularity. However, in the first simulation studies, a uniform structure throughout the whole system is assumed. Figure 9 illustrates the conceptual design of the detector layout.

The calorimeter design is shown in Figure 10. It has a standard sampling structure, with alternating layers of lead and plastic scintillator. One layer consists of 1 mm of lead and 5 mm plastic scintillator. In addition, approximately 1 mm of low-density material will be required for signal routing and photon sensor services. Thus one detector layer is expected to have a thickness of 7 mm. The detector segment inside of the pressure vessel has a thickness of 30 layers. Outside, a thicker detector can be accommodated, presently assumed to be 50 layers thick.

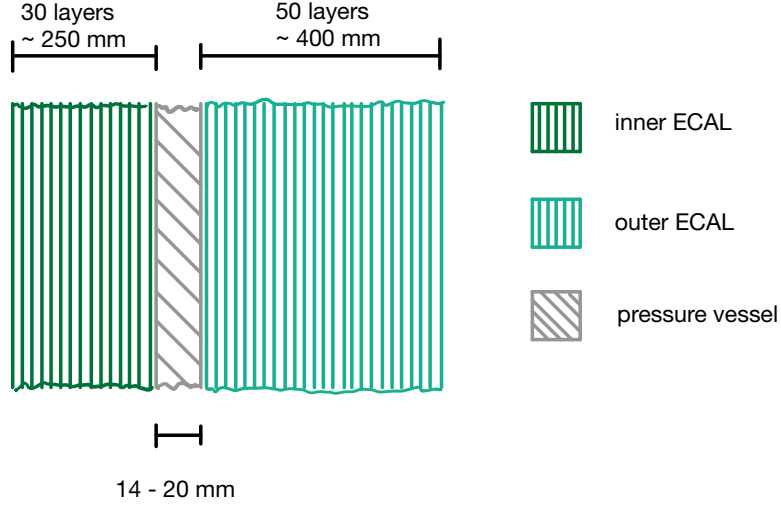


Figure 9: Conceptual layout of the electromagnetic calorimeter, with a segment inside of the pressure vessel of the TPC, and a segment outside.

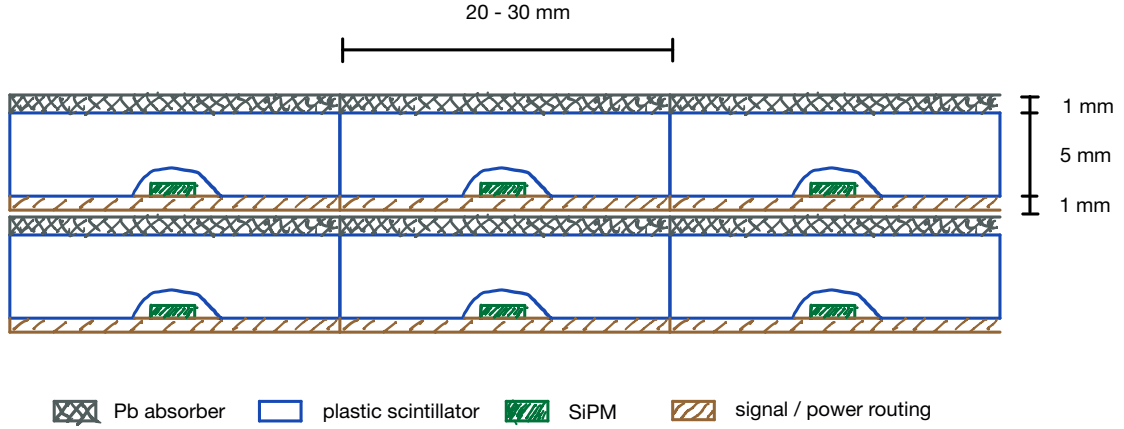


Figure 10: Detail of the conceptual layout of the calorimeter, showing the sampling structure with lead absorber, scintillator and photon sensors and cable routing.

4.5.2 Active elements of ECAL

Simulation studies show that a granularity in the range of $2 \times 2 \text{ cm}^2$ to $3 \times 3 \text{ cm}^2$ provides an optimal performance in terms of photon pointing capability. This can be achieved by a segmentation of the active layers into individual scintillator tiles, each directly read out with a SiPM, making use of the tile designs developed in the context of the CALICE analog HCAL [14, 15]. These scintillator tiles are capable of sub-nanosecond time resolution for single minimum-ionizing particles [16], provided sufficiently fast front-end electronics are used in the system. Figure 11 illustrates the scintillator tile layout.

Using small scintillator tiles throughout the whole calorimeter will result in a relatively high channel count. Other means of achieving comparable effective granularities, such as crossed strips with embedded wavelength shifting fibers, may be a viable solution for large regions of the detector

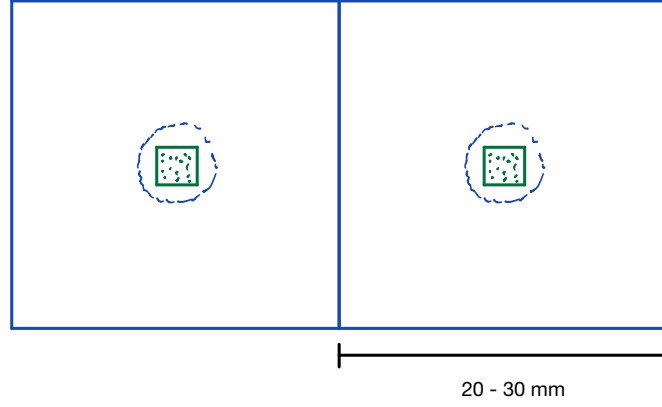


Figure 11: Illustration of the segmentation of the active layers into tiles.

as well.

For first studies, a granularity of $2 \times 2 \text{ cm}^2$ throughout the whole calorimeter is assumed.

4.5.3 Simulated ECAL performance

The expected performance of the calorimeter was studied with GEANT4-based simulations using a simplified detector model and a simplified reconstruction. This study considers only single photons in the ECAL geometry described here. Digitization effects are accounted for by introducing a 150 keV threshold on each detector cell, and a gaussian smearing with a sigma of 100 keV as a first approximation for photon statistics and electronic noise. Two different scenarios for the pressure vessel are studied:

- A stainless steel vessel, with a thickness of approximately $1 X_0$, simulated as a 2 cm thick steel layer
- A titanium vessel, with a thickness of approximately $0.4 X_0$, simulated as a 1.4 cm thick titanium layer

As visible in the results presented in the following, the type of pressure vessel has only a small impact on the pointing resolution of the detector, but has a significant influence on the energy resolution, as discussed below. It must be noted that at present no extra material between the inner calorimeter and the pressure vessel is included in the simulations, although some mechanical infrastructure as well as readout electronics will be required there.

Pointing resolution The direction resolution of the calorimeter has been studied with a very simple algorithm, which is based on a two-stage direction fit. As a first step, the direction of the main axis of the ensemble of cells above threshold is determined with a principal component analysis. This direction is then taken as the starting value for a three-dimensional line fit through the center of gravity of the energy deposit in each layer. The resolution is primarily driven by the energy deposits in the first segment of the detector, so the choice of the material of the pressure vessel does not have a significant impact on the performance. In general, a higher granularity leads to a better

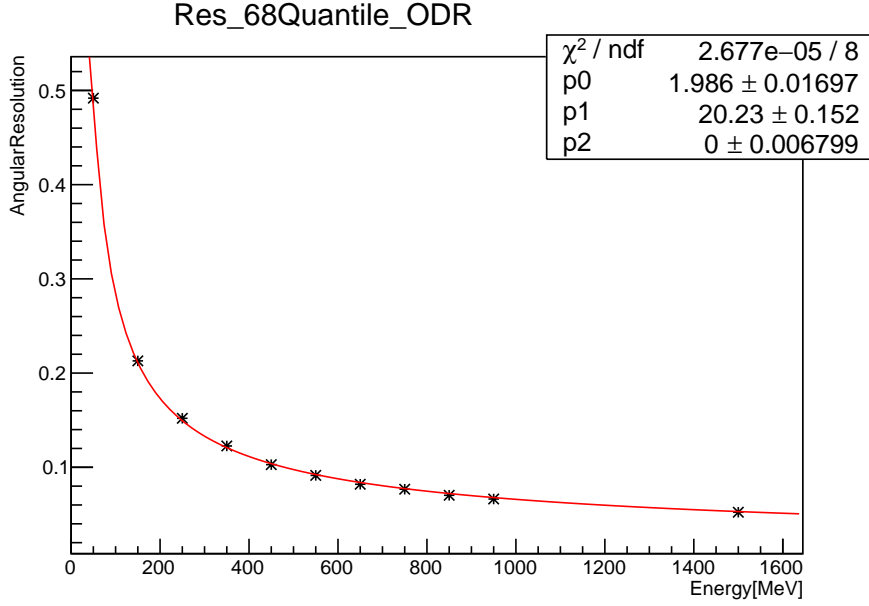


Figure 12: Angular resolution in radians as a function of photon energy for the case with a titanium pressure vessel, showing the 68 percentile. The fit function is $\sqrt{p_0^2/E + p_1^2/E^2 + p_2^2}$.

performance, but first studies indicate that the improvement for cells smaller than $20 \times 20 \text{ mm}^2$ is not significant.

Figure 12 shows the angular resolution of the calorimeter in the scenario with a titanium pressure vessel. It is expected that an improvement of the resolution can be achieved with a more sophisticated reconstruction technique, which should outweigh the possible overestimation of the performance due to the simplifications of the present study.

Energy resolution The energy resolution is determined from a gaussian fit to the visible energy in the scintillator. In this simplified procedure, corrections in the region of the pressure vessel, which are required to fully recover a linear response of the detector, are neglected. At the same time, more sophisticated techniques for the energy reconstruction, which account for the information lost in the pressure vessel, for example by fitting a shower profile, are also not yet implemented. While the former would lead to a slight deterioration of the energy resolution, the latter should result in an improvement.

Figure 13 shows the energy resolution of the simulated calorimeter for the detector design with a titanium vessel. The fit function, which corresponds to the standard parametrization of the calorimeter energy resolution with a stochastic, a noise and a constant term, does not well describe the observed behavior of the resolution. This is due to the energy dependence of the impact of the pressure vessel, which affects higher energies more than low energies, since the region of the shower maximum moves into the vessel region for energies of 1 GeV and higher. At low energies, the resolution is close to $5\%/\sqrt{E/\text{GeV}}$, while for energies above 1 GeV, it is slightly above $6\%/\sqrt{E/\text{GeV}}$, approaching $7\%/\sqrt{E/\text{GeV}}$ at 1.5 GeV. It should be noted that, due to the absence of the simulation of non-uniformities, dead region, more extensive noise and photon statistics effects and the like,

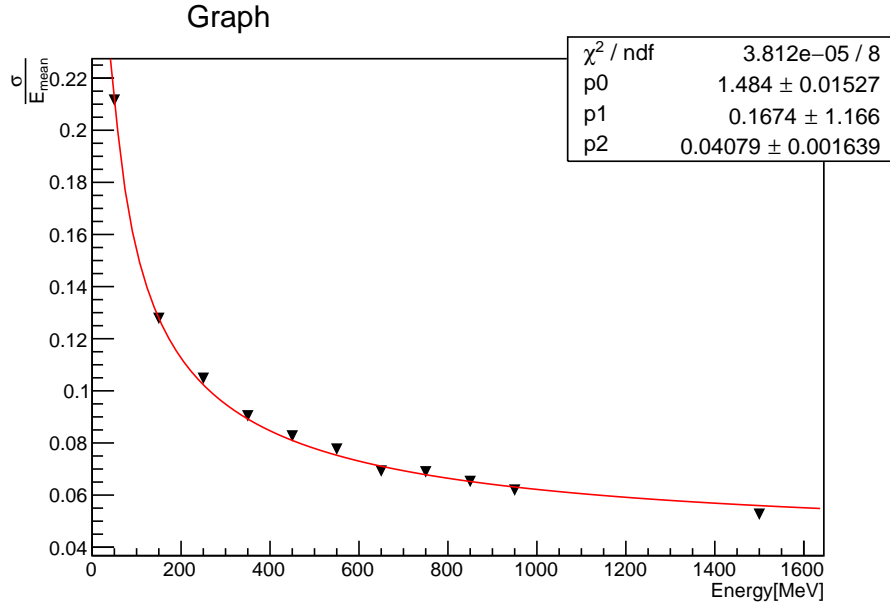


Figure 13: Energy resolution as a function of photon energy for the case with a titanium pressure vessel, determined by a gaussian fit to the visible energy in the scintillator. The fit function is $\sqrt{p_0^2/E + p_1^2/E^2 + p_2^2}$, but the interpretation in terms of the usual terms of a calorimeter energy resolution does not work due to the energy dependence of the impact of the pressure vessel. The fit parameters can thus be used to as a parametrization of the resolution, but not to interpret the performance of the detector as such.

the energy resolution is overly optimistic in the simulations, with realistically achievable numbers probably 20% to 30% worse. The addition of more dead material between the first calorimeter segment and the pressure vessel will also negatively affect the resolution.

Figure 14 shows the energy resolution of the ECAL for different options of the pressure vessel. This illustrates the substantial benefits of a titanium vessel for the energy resolution, in particular for higher photon energies. Using titanium, the resolution is much less degraded relative to the case of an uninterrupted calorimeter than when using stainless steel.

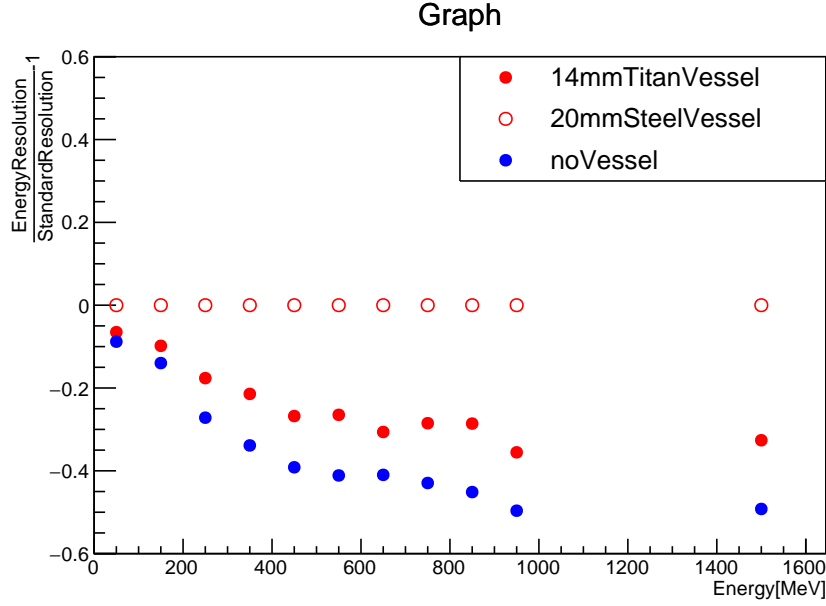


Figure 14: The energy resolution of the ECAL for different scenarios of the pressure vessel, relative to the case for a steel vessel with a thickness of 2 cm.

4.6 Neutron detection capabilities

In order to study the neutron detection capabilities of the HPgTPC, a MARS [17] simulation was used. The basic geometry consisted of a 5 m diameter by 5 m long cylinder filled with a 90-10 Ar-CH₄ mixture at a pressure of 10 Atm (1.7×10^{-2} g/cm³). Neutrons with kinetic energy between 25 MeV and 500 MeV were shot into the HPgTPC volume and neutron interactions that produced a proton or a deuteron were used to produce histograms of E_p and E_d . A 5 MeV K.E. threshold was required in order to claim detectability of the neutron interaction by observation of the proton or deuteron. Figure 15 shows a typical 100 MeV neutron interacting on Ar producing a proton in the final state. The particle types are color coded as indicated in Figure 6. The incoming (from the left) 100 MeV neutron produces a 14 MeV (K.E.) proton with an outgoing 6.5 MeV neutron and 1.4 MeV gamma. An interaction producing a deuteron is shown in Figure 16. In order to determine the neutron detection efficiency as a function of incident neutron energy, neutron interactions in the gas that produced a proton or a deuteron were tagged and histograms of the proton and deuteron energy distributions were produced. Each run consisted of 5000 beam neutrons. The probability of producing a deuteron was $\simeq \frac{1}{3}$ that of producing a proton. The data for protons (energy scale in GeV) are shown in Figure 17. Figure 18 gives the efficiency for detecting a neutron as a function of neutron energy if a proton was produced, if a deuteron was produced, and finally if either a proton or deuteron were produced.

4.6.1 Discussion

Figure 18 shows that the direct detection efficiency for fast neutrons in the Ar-CH₄ gas is quite small. Determining the energies carried away from the primary vertex by neutrons on an event-by-event basis will not be possible in the HPgTPC. However, given the unmatched tracking resolution at very

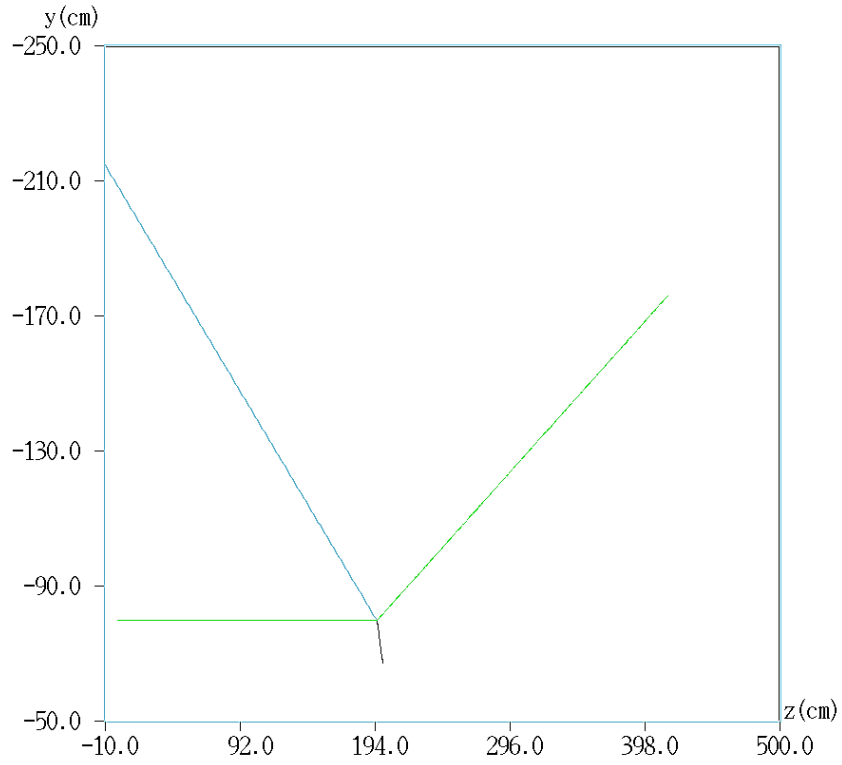


Figure 15: 100 MeV neutron interaction on Ar producing a proton a neutron and a gamma.

low (≈ 5 -10 MeV) particle energy, the HPgTPC will be able to tag neutron interactions better than any other detector technology currently under consideration, by detecting the recoiling protons or deuterons from neutron scatters. Given the large number of events produced in the TPC, neutron energy distributions binned in relatively broad neutrino energy bins can be produced. These, along with proton energy distributions from the vertex, plus modeling, may allow us to produce an improved model for the energy carried away by neutrons based on the visible vertex activity.

Measuring the missing energy due to neutrons will be extremely difficult with any of the technologies under consideration. Being able to tag a neutron event and then measure the outgoing proton's (deuteron's) direction and energy can yield an accurate determination of the incident neutron's energy. To do this with high efficiency is a tremendous challenge.

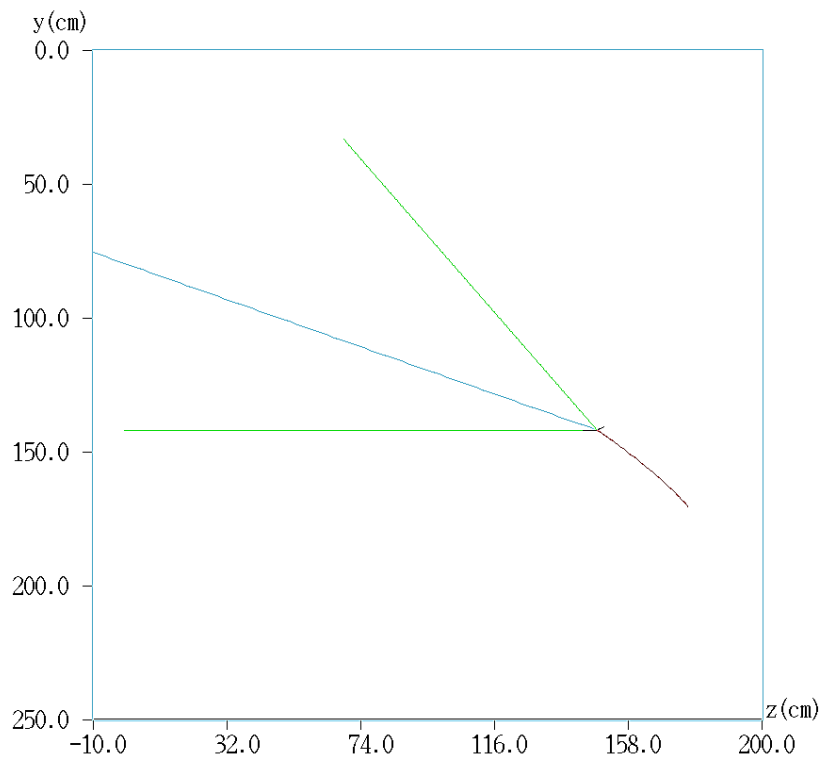
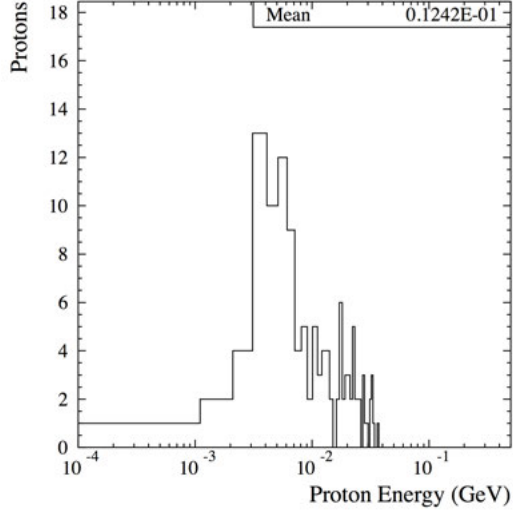
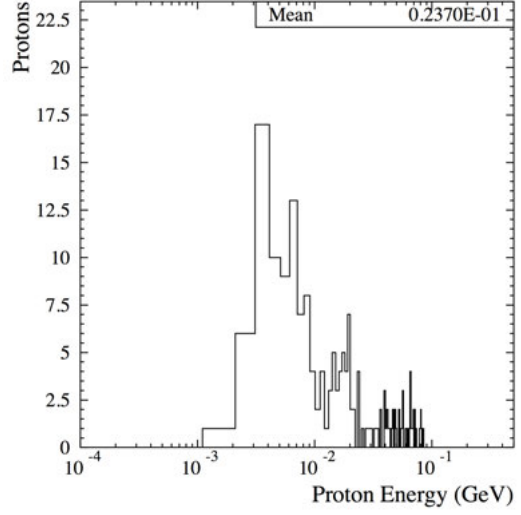


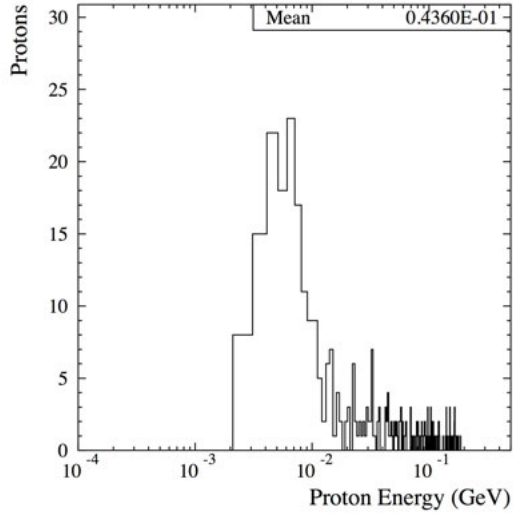
Figure 16: Deuteron in the final state.



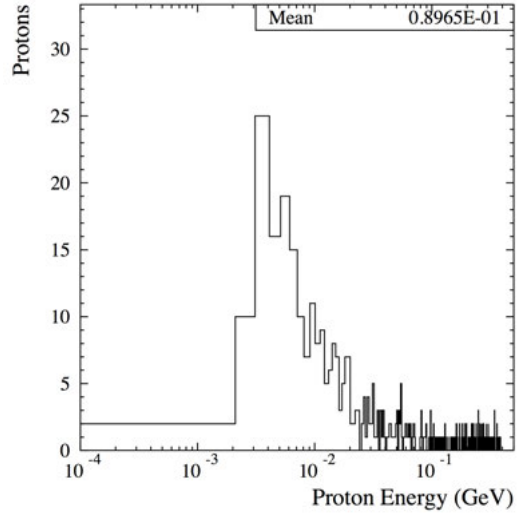
(a) Proton E dist. for 50 MeV neutrons



(b) Proton E dist. for 100 MeV neutrons



(c) Proton E dist. for 200 MeV neutrons



(d) Proton E dist. for 400 MeV neutrons

Figure 17: Proton energy spectra for neutrons of 50, 100, 200 and 400 MeV K.E.

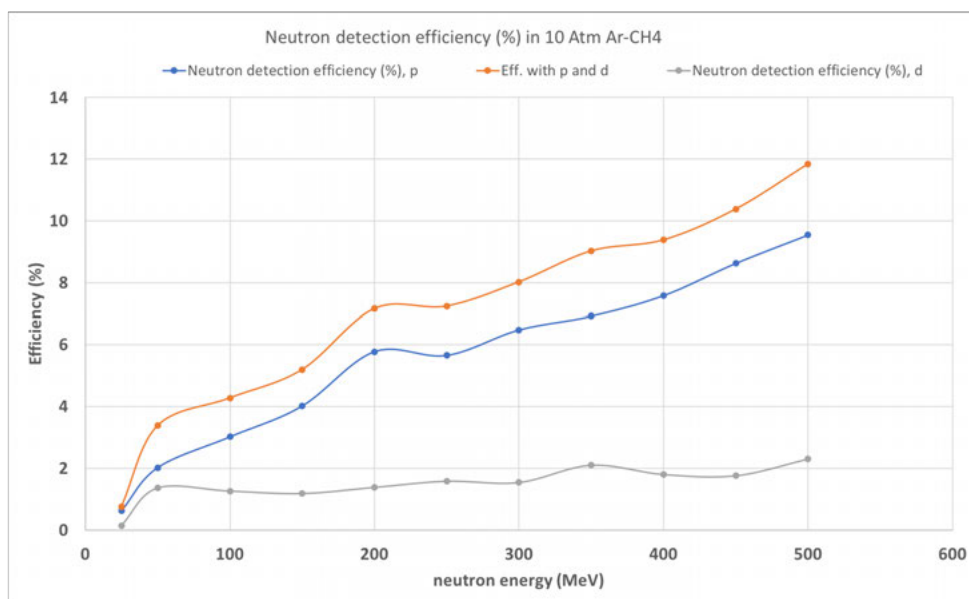


Figure 18: Neutron detection efficiency.

4.7 Performance for key channels

4.7.1 Energy Resolution of ν_μ CC Events as a Function of Detection Threshold

To study the neutrino energy resolution in ν_μ CC, samples of GENIE events [10, 11] were generated. Four samples were generated: 10,000 inclusive ν_μ events on ^{40}Ar , 10,000 inclusive $\bar{\nu}_\mu$ events on ^{40}Ar , and for comparison, 10,000 inclusive ν_μ events on ^{12}C and 10,000 inclusive $\bar{\nu}_\mu$ events on ^{12}C . The energy spectrum for the events was a parameterization in the range $0.5 < E_\nu < 3.0$ GeV, with a differential distribution proportional to $E_\nu^2 e^{-1.5E_\nu}$, which is designed to peak at around 2 GeV and sample the relevant energy range around the first oscillation maximum.

The effect of lowering the detection threshold was studied by assuming perfect efficiency, particle ID, and resolution to detect and measure particles above the desired energy threshold. The neutrino energy was reconstructed as E_{vis} , which is the sum of the following terms:

- The total energies of electrons and muons if $E_{\text{kin}} > E_{\text{thresh}}$,
- The total energies of charged pions if $E_{\text{kin}} > E_{\text{thresh}}$,
- The total energies of neutral pions, and
- The kinetic energies of protons if $E_{\text{kin}} > E_{\text{thresh}}$.

In addition to E_{vis} , another quantity, $E_{\text{vis,w/neutrons}}$ is computed, adding in the kinetic energies of all neutrons emitted from the primary vertex in the GENIE events, without a kinetic energy threshold requirement. Other particles are ignored. Neutral K mesons and Λ baryons are not decayed by GENIE and are neglected in this study. Nuclear fragments also are ignored. The effect of nuclear binding energy is also not included in the energy reconstruction, but is included in GENIE's simulation. The energy thresholds investigated were 50 MeV, 20 MeV, 5 MeV, and 2.5 MeV. The fractional energy residual is defined to be

$$R_E = \frac{E_{\text{vis}} - E_\nu}{E_\nu} \quad (4.1)$$

where E_ν is the true neutrino energy in the GENIE event. A similar residual, $R_{E,\text{neutrons}}$ is defined using $E_{\text{vis,w/neutrons}}$.

Table 4 lists the mean value and RMS of the two energy residuals R_E and $R_{E,\text{neutrons}}$, as functions of the threshold, separately for ν_μ CC events and $\bar{\nu}_\mu$ CC events. They are tabulated separately because of the dominance of an energetic recoiling proton in the neutrino case and an energetic recoiling neutron in the antineutrino case. The average energy residual and its RMS value are only weakly dependent on the kinetic energy thresholds for low-energy protons. While GENIE predicts many low-energy protons, they do not contribute a large amount to the neutrino energy reconstruction. Figures 19 shows the distributions of R_E and $R_{E,\text{neutrons}}$ for E_{thresh} cuts of 2.5 MeV and 50 MeV, for ν_μ CC and $\bar{\nu}_\mu$ CC events on ^{40}Ar . The dominant effect on the energy scale and energy resolution in all cases is the lack of neutron energy reconstruction. Including low-energy protons is a smaller contribution.

Table 4: Mean and RMS energy residuals for neutrino events on ^{40}Ar .

Sample	E_{thresh}	$\langle R_E \rangle$	RMS R_E	$\langle R_{E,\text{neutrons}} \rangle$	RMS $R_{E,\text{neutrons}}$
$\nu_\mu\text{CC}$	2.5 MeV	-0.111	0.138	-0.019	0.052
$\nu_\mu\text{CC}$	5.0 MeV	-0.112	0.138	-0.020	0.052
$\nu_\mu\text{CC}$	20 MeV	-0.117	0.140	-0.025	0.054
$\nu_\mu\text{CC}$	50 MeV	-0.130	0.146	-0.037	0.063
$\bar{\nu}_\mu\text{CC}$	2.5 MeV	-0.128	0.122	-0.018	0.044
$\bar{\nu}_\mu\text{CC}$	5.0 MeV	-0.129	0.122	-0.018	0.044
$\bar{\nu}_\mu\text{CC}$	20 MeV	-0.132	0.123	-0.022	0.046
$\bar{\nu}_\mu\text{CC}$	50 MeV	-0.141	0.127	-0.030	0.051

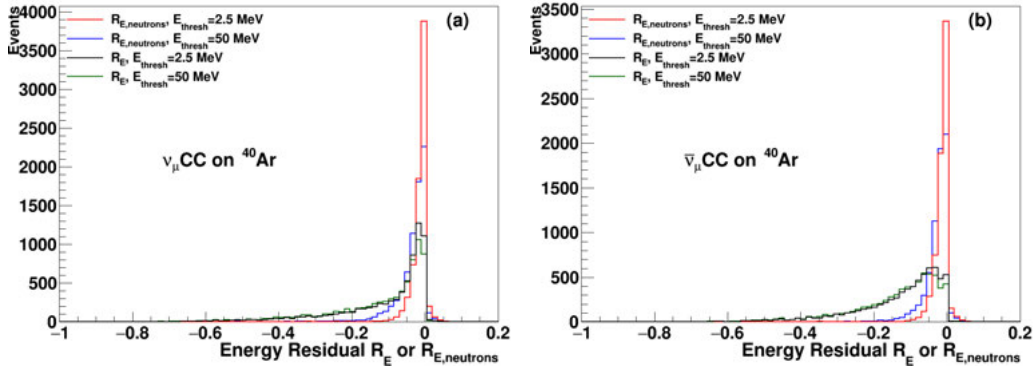


Figure 19: Distributions of R_E and $R_{E,\text{neutrons}}$, with $E_{\text{thresh}} = 2.5$ MeV and 50 MeV for (a) $\nu_\mu\text{CC}$ and (b) $\bar{\nu}_\mu\text{CC}$ events.

4.7.2 Distinguishing among nuclear models in neutrino interaction generators

A long-standing question in neutrino interaction generators is that of the multiplicities and energy spectra of nucleons ejected from the nucleus as a result of the interaction. A comparison of the output from three different neutrino interaction generators, GENIE, NEUT, and NUWRO, shows significant differences in the spectra of outgoing protons, since the underlying nuclear models and implementations in these generators are different. The HPgTPC's advantage of a lower threshold for detection of low energy protons, indicated by the solid black vertical line at 5 MeV shown in Figure 20, makes it well-suited to distinguishing among models and making measurements that will allow model-builders to refine their generators. By comparison, the detection threshold in LAr (shown by the dashed black vertical line at 40 MeV in the same figure) is too high to be sensitive to the regions where models differ greatly in their predictions.

4.7.3 CC and NC Coherent Pion Production

As the coherent pion production cross sections are the same for neutrinos and antineutrinos, measurement of coherent pion cross sections in the two running modes gives an opportunity to check for any biases in neutrino vs. antineutrino measurements. These events can also be used to

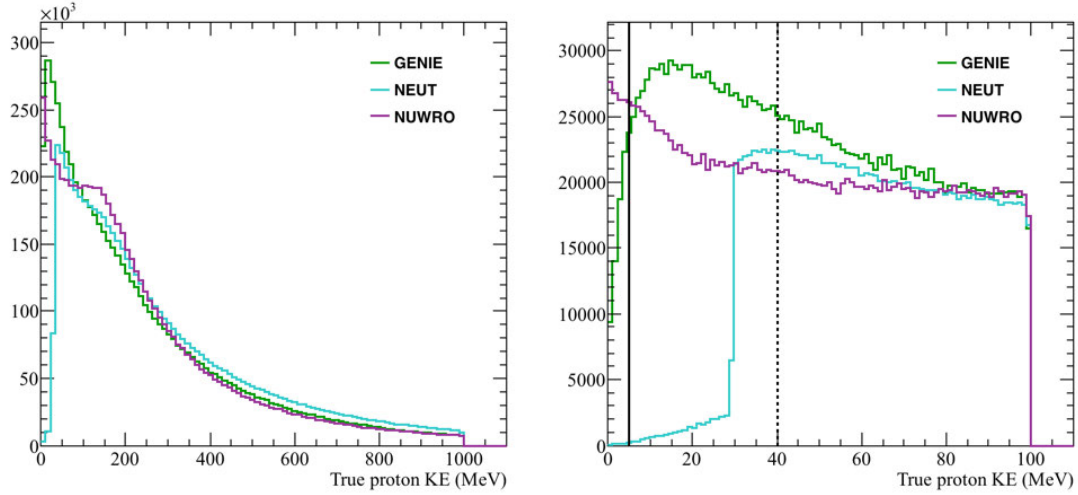


Figure 20: Predicted proton energy spectra from GENIE, NEUT, and NUWRO. Energy spectra up to 1 GeV are shown on the left, and zoomed in to lower energies on the right. The dashed vertical line indicates the proton detection threshold for a LArTPC, and the solid vertical line shows the threshold for an HPgTPC. The lower detection threshold in the HPgTPC provides a unique opportunity to distinguish among the models for the same nuclear target as the ND and FD LArTPCs.

estimate the true neutrino energy for both neutrinos and antineutrinos, as there is almost no energy transferred to the nucleus and no additional particles produced in the interaction.

The statistics are somewhat low in the HPgTPC (8k CC + 5k NC coherent pion events per year in neutrino mode), but the low threshold for detection of vertex activity allows selection of a cleaner sample of events in the gaseous argon than in the liquid argon, where low energy vertex activity is more easily missed.

In a sample of 745k non-coherent CC events generated on argon via a stand-alone GENIE simulation with DUNE flux, we did a truth-level study of hadronic vertex activity to determine what fraction of events could mimic coherent pion interactions, assuming particle detection thresholds of 40 MeV kinetic energy in the LArTPC and 5 MeV in the HPgTPC. Table 5 shows the results of this study. In the LArTPC, 407 (0.05%) of the original 745k events passed the selection cuts, meaning that they would mimic a coherent pion (all other hadrons have kinetic energies below the chosen detection threshold of 40 MeV). In the HP GArTPC, only 8 (0.001%) of the original 745k events passed the selection cuts for a threshold of 5 MeV. In one year of running, this would be only 16 background events, compared to the 8000 signal events.

Detecting NC coherent pion production in the HPgTPC is more difficult, since the only activity should be in the ECAL. Coherently produced neutral pions should have no vertex activity; they should have only a single π^0 (usually forward-going). Since the π^0 's decay photons do not convert in the low-density gas volume of the HPgTPC, the event signature would be shower activity in the ECAL alone, although with good enough pointing resolution from the ECAL, a veto on low-energy protons near the projected vertex location in the HPgTPC would give a very clean sample of these events as well. From studies done during the Near Detector Task Force, it is expected that less than

Table 5: CC coherent pion MC truth level analysis. Fraction of events that would be classified as CC coherent pion events, assuming detection threshold for charged particles in a LArTPC is 40 MeV. For the HP GAr TPC, a conservative threshold of 5 MeV and an improved threshold of 2.5 MeV are shown. Ignoring the pion with the most energy, all other hadrons are required to have energies below the detection threshold to qualify as background to CC coherent pion interactions.

	Coherent-like Events (Fraction passing cuts)
All non-coherent CC events (no cuts)	745720 (1.0)
LArTPC ($E_{\text{thresh}} = 40$ MeV)	407 (0.0005)
HPgTPC ($E_{\text{thresh}} = 5$ MeV)	8 (1×10^{-5})
HPgTPC ($E_{\text{thresh}} = 2.5$ MeV)	1 (1×10^{-6})

1% of events will have additional activity occurring in the ECAL within 50 ns (uncertainty in the vertex position within the TPC, due to spill duration) of a neutrino interaction in the HPgTPC.

4.7.4 Low- ν Events

The same arguments for better detection of low-energy vertex activity apply also in the case of a low- ν analysis; the HPgTPC will collect a cleaner sample of low- ν events on an argon target than the other detector technologies under consideration.

A truth-level study of low- ν interactions is shown in Table 6. For this study, 1 million NC and CC GENIE events were generated according to the DUNE ND flux. In each event, only *visible* hadronic energy was summed to determine if the event would have been classified as low- ν ; neutrons are ignored for both detectors. The detection threshold for charged particles in the LArTPC is assumed to be 40 MeV, and in the HPgTPC the sample purity is assessed for two detection thresholds: 5 MeV and 2.5 MeV, based on range arguments that were discussed earlier in Section 4.3.

Table 6: Low- ν MC truth level analysis. Fraction of events that would be classified as low- ν , assuming detection threshold for charged particles in a LArTPC is 40 MeV. For the HPgTPC, a conservative threshold of 5 MeV and an improved threshold of 2.5 MeV are shown.

	Low- ν [$E_{\text{had}} < 250$ MeV] Events (Sample Purity)	Low- ν [$E_{\text{had}} < 100$ MeV] Events (Sample Purity)
True visible E_{had} (no cuts)	268523 (1.0)	137479 (1.0)
LArTPC ($E_{\text{thresh}} = 40$ MeV)	283226 (0.95)	154884 (0.89)
HPgTPC ($E_{\text{thresh}} = 5$ MeV)	269072 (0.998)	138385 (0.993)
HPgTPC ($E_{\text{thresh}} = 2.5$ MeV)	268665 (0.999)	137720 (0.998)

4.7.5 Background to ν_e Charged Current Interactions

The benefit of the HPgTPC is more clear in the larger context of an integrated argon near detector, with an upstream LArTPC plus a magnetized downstream HP gaseous argon TPC. The HPgTPC

itself will make a background-free measurement of the rate of intrinsic beam ν_e CC interactions on argon (approximately 19k events per year in the fiducial volume). In the iArDet configuration, the ability to measure ν_e CC interactions in two different TPCs, both with argon as the target material, also provides a way to constrain backgrounds of the LArTPC measurement that will not be mistakenly classified as ν_e signal in the GARTPC. This is discussed in more detail in Section 5.

4.8 Full pattern recognition and reconstruction utilizing ALICE code framework

The ALICE collaboration has made their offline framework and analysis software available on github [18]. The code has been successfully compiled and run on a Mac laptop, placing individual particles in the TPC region of the full ALICE detector. The next step is to place full neutrino interactions in the TPC and evaluate the performance of the reconstruction software for interactions originating inside the TPC. In principle, this should not require any code modifications, since the first pass of ALICE TPC reconstruction uses information from the TPC only, with no constraints or inputs from the other subdetectors of ALICE.

5 Performance of integrated Ar detector, iArDet: ArgonCube + HPgTPC

In this section, we discuss the benefits of a downstream high-pressure gaseous argon TPC working in conjunction with the upstream LArTPC.

5.1 Cross section measurements on argon in a magnetized detector

The LArTPC will measure neutrino-argon and antineutrino-argon interaction cross sections with high statistical precision, but the HPgTPC adds valuable contributions to these measurements due to:

- The same target material, argon (97% of interactions)
- Event-by-event charge sign determination for $\nu/\bar{\nu}$ discrimination
- Better vertex resolution for identification of low energy particles ejected from the nucleus.

The event rates for CC and NC interactions in the HPgTPC are substantial: 1.64M CC events and 517k NC events per year of running with 1-ton fiducial mass. In addition, our advancement in the integrated design of ArgonCube + the HPgTPC, as shown in section A.1.4 and in Figure 24, supports our arguments regarding the effective coupling of the two systems.

5.2 Intrinsic ν_e rate measurement and constraining backgrounds to LArTPC interactions

In the near detector complex, an accurate measurement of the intrinsic beam ν_e 's and relevant backgrounds is a useful input for Far Detector oscillation analyses. The iArDet provides a unique capability to constrain backgrounds that are misidentified as ν_e CC in the LArTPC, since the HPgTPC will collect a background-free sample of 19k ν_e CC events, which will also have wrong-sign tagging from the magnetic field.

Preliminary ν_e CC selection studies in the MicroBooNE LArTPC indicate that backgrounds to this sample are primarily due to misidentification of ν_μ NC π^0 events. In contrast, the HPgTPC

measurement will have essentially no background due to NC π^0 events, as the π^0 s do not convert in the gas volume, and the 1% of NC π^0 events with Dalitz decays will be easily tagged by the oppositely-bending e^+ and e^- tracks. A clean measurement of the ν_e CC rate in the HPgTPC, despite its lower statistical precision, constrains the backgrounds in the higher statistics ν_e CC-like measurement made in the LArTPC, since the target nucleus is the same in both detectors. The measured rate of ν_e CC intrinsic events is also directly applicable to Far Detector analyses.

In the ArgonCube fiducial volume, we expect approximately 214k true ν_e CC events per year plus some number of background events. MicroBooNE preliminary studies point to misidentification of NC π^0 events as one of the larger contributions to ν_e CC backgrounds. To investigate this further, we undertook a truth-level study of 1M CC and NC neutrino interactions on argon generated with GENIE and the DUNE flux. GENIE predicts that 19% of NC π^0 events have no additional hadronic vertex activity (making these types of events more likely to have a mis-reconstructed vertex location at the start of a photon conversion instead of the true vertex, and which, if one photon is missed, may be more easily mistaken for ν_e CC). The majority of NC π^0 events do have additional vertex activity, however. Approximately 12% of GENIE NC π^0 events with vertex activity will have only hadrons below the assume LArTPC detection threshold of 40 MeV, which places them also into the category of events that may be mistaken for ν_e CC in the LArTPC, if one photon is missed. In the HPgTPC, none of the π^0 s will convert in the gas volume, and so these events can be rejected by requiring no activity in the ECAL.

Constraining backgrounds to other cross section measurements made in the LArTPC will also be possible with the HPgTPC.

5.3 HPgTPC acceptance for muons originating in ArgonCube

[Work in progress.]

The HPgTPC will assist the LArTPC in the measurement of neutrino interactions by tracking particles escaping the liquid and determining, with high resolution, their momentum. The geometric acceptance of the system was estimated with a detector simulation that includes a detailed description of the ND geometry (see Figure 21).

The GENIE Monte Carlo event generator (version 2.12.6 with CC/NC MEC physics model enabled) was used to generate a large sample (7.5E17 POT equivalent) of neutrino interactions in the active volume of the LArTPC. The final-state particles in these interactions were then propagated through the ND detector geometry down to zero range using the Geant4-based EdepSim application, and in their interactions with the detector materials further particles may be generated. The trajectories and associated energy deposits of charged particles in the various active volumes of the near detector (i.e. the TPCs and the active layers of the ECAL) are recorded as hits and written to an output file together with the genealogy of each simulated particle.

Figure ?? shows the fraction of primary particles generated in a neutrino interaction in the LArTPC that enter the HPgTPC as a function of their initial position. The fraction of particles for which a reliable momentum measurement can be performed (tracks in the HPgTPC longer than 1 meter) is shown in Figure ??.

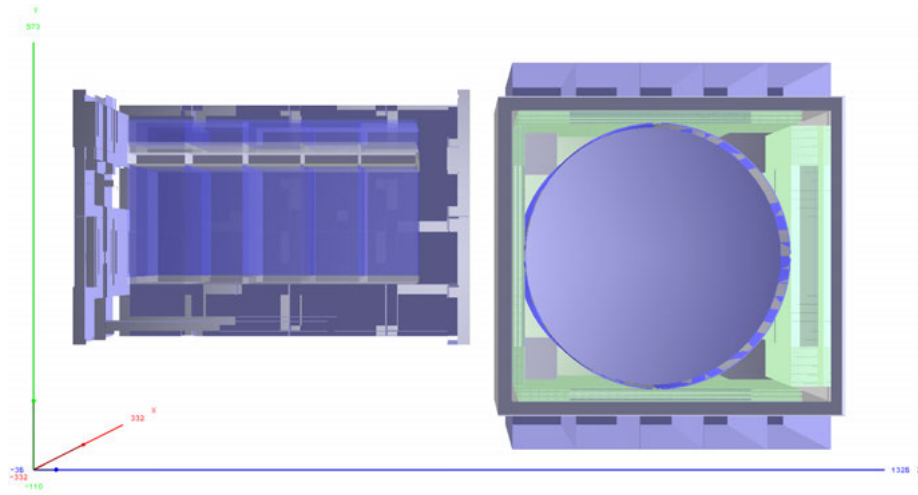


Figure 21: The geometry of the DUNE ND as implemented in the detector simulation.

6 Conclusions

The integrated argon detector described in this report presents an opportunity not only to make stand-alone measurements of importance to the neutrino community, but also to enhance the measurements made in the upstream ArgonCube LArTPC. The 1 t fiducial mass of the HPgTPC that is possible with the dipole magnet configuration will collect a substantial number of neutrino interactions for cross section measurements on an argon target: 1.6 million charged current interactions, and more than 500k neutral current interactions per year of exposure. The improved vertex resolution provided by the HPgTPC also offers a unique opportunity to disentangle differences among neutrino interaction generators regarding multiplicity and energy distributions of low energy particles ejected from the nucleus on the same target material as the near and far detector LArTPCs. Measurements in the HPgTPC will also be useful for constraining backgrounds to some exclusive interaction channels measured at in the LArTPC, such as coherent pions and low- ν . With the engineering design of a G10 (or carbon-fiber) window in the downstream wall of the cryostat, and the improved magnet design discussed in Appendix A, the material budget between the upstream LArTPC and the downstream HPgTPC is reduced significantly, making a truly integrated Ar-target near detector a feasible option.

Appendices

A Towards a fully integrated Argon detector design

In order to maximize the complimentary of the FGT (in this case the HPgTPC) and ArgonCube, a configuration that minimizes the amount of dead material between the two system is of paramount importance. The following sections enumerate how we plan to accomplish this, working from ArgonCube to the HPgTPC.

A.1 Thin-wall cryostat for ArgonCube

In this appendix, we describe a design for a thin-walled (in radiation lengths) downstream cryostat wall (facing HPgTPC) for ArgonCube.

A.1.1 Introduction

This appendix is a design proposal for the ArgonCube cryostat. The design of ArgonCube is modeled off the 35 t cryostat, which is currently operational at Fermilab. The 35 t cryostat (US short tons) is a membrane cryostat that consists of a thin layer of corrugated stainless steel followed by insulation and concrete. The goal of the ArgonCube design is to minimize the radiation length of one cryostat wall. This can be accomplished by creating a “window” in one wall and replacing the concrete with a thinner material, such as G10. G10 was the primary material analyzed for this report. However, we have also considered a design with a carbon-fiber composite wall that reduces the thickness in radiation lengths (relative to G10) by almost a factor of 3.

A.1.2 Membrane Cryostat Background Information

Membrane cryostats consist of a very thin layer of corrugated stainless steel (the membrane) surrounded by a structural support system and insulation. The membrane design, shown in Figure 22, allows for expansion and contraction of the stainless steel wall, which is typically a few millimeters thick. Membrane cryostats have been successfully used for transportation and storage in the liquid natural gas (LNG) industry since 1959 [19]. With advancing technology, tanker ships now have the capacity to carry up to 266,000 m³ of LNG in membrane vessels [20].

A.1.3 35-ton Experiment- Summary of Successfully Built Membrane Cryostat

Fermilab built a membrane cryostat for the 35 t experiment (35T) in 2013. IHI Corporation designed the membrane cryostat and oversaw the installation process at Fermilab. The 35 t cryostat, with a volume of 29 m³, was built as a prototype to determine if membrane tank technology would meet the scientific and engineering requirements of the LBNF/DUNE project. Factors taken into consideration during the design and construction processes were thermal performance, feasibility for liquid argon, argon purity, and leak tightness [21]. These goals were successfully met. The heat leak through the cryostat walls, calculated by Terry Tope, was found to equal 11.5 W/m² [22]. The 35 t cryostat has proven to be feasible for liquid argon use and has been operational since 2014. High purity levels of liquid argon, more than 1.4 millisecond electron lifetimes, were achieved by circulating the liquid argon through an external filtration system [21]. The two filters, the first containing a molecular sieve and the second containing copper pellets, remove water and

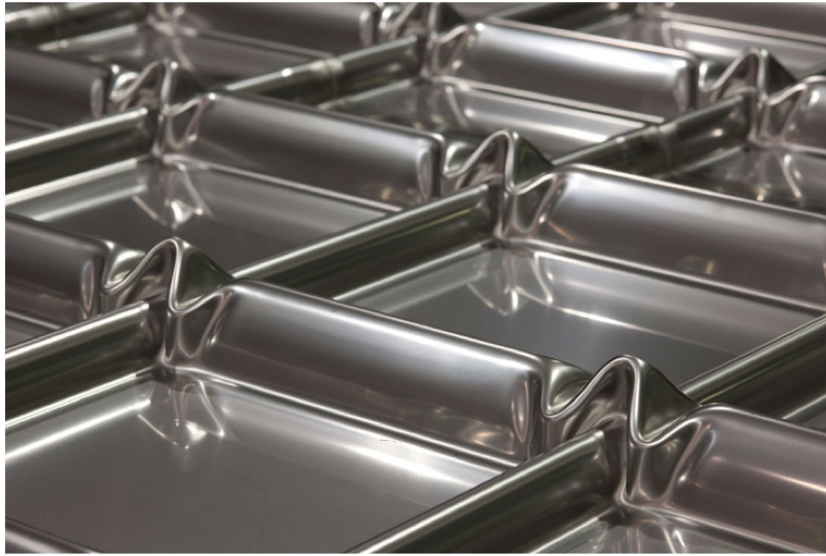


Figure 22: Section of membrane wall at Fermilab [3]

oxygen impurities from the liquid argon. During the initial cryostat pressure test, a leak check was performed on the membrane and no leaks were found [21].

There are eight layers that make up the 35 t vessel walls. The layers are summarized in Figure 23, below. Terry Tope's pressure vessel engineering note on the 35T cryostat contains the

Layer	Material	Thickness (mm)
Membrane	304 Stainless Steel	2
Fireproof board	Calcium Silicate board	10
GRE/GRU	Glass reinforced epoxy/glass reinforced urethane	0.01
Insulation	High temperature polyurethane foam	190
GRE/GRU	Glass reinforced epoxy/glass reinforced urethane	0.01
Insulation	High temperature polyurethane foam	200
Moisture Barrier	Carbon Steel	1.2
Reinforced Concrete	Reinforced concrete	300

Figure 23: Membrane cryostat layers in 35 t vessel

structural calculations and testing of the concrete. Cured concrete cylinders were tested 5, 7, and 28 days after being poured. The resulting 28-day compressive strength was 35.9 MPa (5,213 psi), which met the 34.5 MPa (5,000 psi) requirements for 35T [22]. The design pressure of 35T is 20.6 kPa (3 psig) at -189°C (-309°F).

A.1.4 Design Proposal for ArgonCube Cryostat

The basis of the ArgonCube cryostat design stems from the design of the 35 t vessel. The proposal is to build a membrane vessel for ArgonCube with the same (or similar) cryostat walls as 35 t. A critical design component of the ArgonCube cryostat is reducing the radiation length through one of the cryostat walls. The goal is to achieve a thickness of 0.5 radiation lengths. This minimized

radiation length is only important for the cryostat wall between the liquid and gas vessels (see Figure 24). Calculations determined that thickness of the 35 t vessel is equivalent to 2.9 radiation lengths. The largest contributing factor to this high radiation length is the concrete layer. Figure 25 shows the layers and corresponding radiation lengths. A layer of G10 instead of concrete is

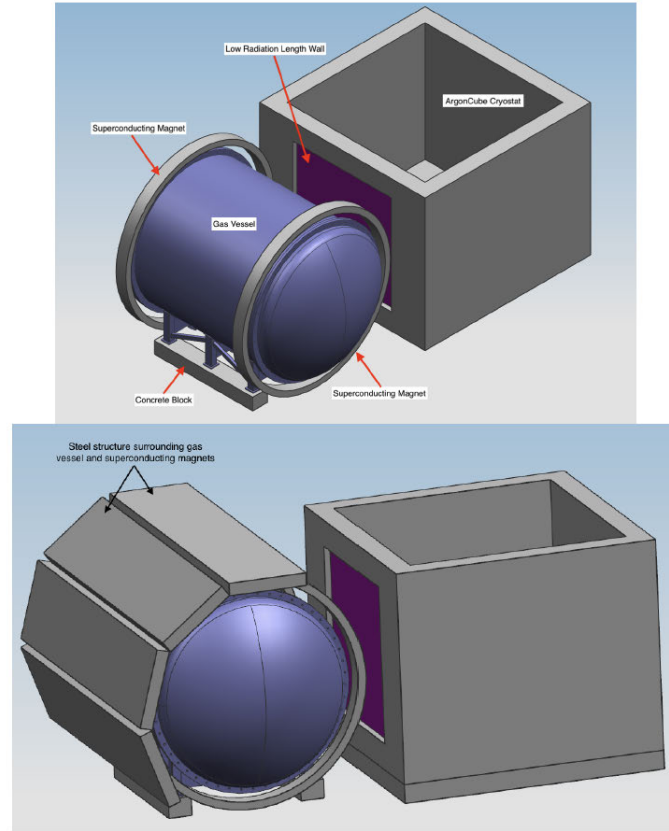


Figure 24: ArgonCube cryostat, TPC pressure vessel with modified dipole magnet (see section A.2). The upper figure shows the ArgonCube cryostat, the HPgTPC pressure vessel and the superconducting coil cryostats. The lower figure adds a concept for the return iron.

Layer	Radiation Length based on Material Composition		Density	Thickness	Calculated Radiation Length	Percentage of Total Radiation Length
	g/cm^2	mm	g/cm^3	mm	unitless	%
304 SS Membrane	13.904	17.6	7.9	2	0.11	3.95
Fireproof Board	23.955	399.25	0.6	10	0.03	0.87
Insulation 1st Layer	40.8	5440	0.075	190	0.03	1.21
Insulation 2nd Layer	40.8	5440	0.075	200	0.04	1.28
Carbon Steel	7.85	17.60	7.9	1.2	0.07	2.37
Concrete	28.875	115.5	2.5	300	2.60	90.31
Total Radiation Length					2.88	100.00

Figure 25: Layers in 35 t cryostat vessel in units of radiation length.

proposed for the ArgonCube cryostat to maintain structural requirements and minimize radiation

length. The layers of the ArgonCube cryostat, including the G10 window, are shown in Figure 26. A $5\text{ m} \times 5\text{ m} \times 0.1\text{ m}$ window of G10 would be fixed within the surrounding concrete wall (see Figure 27). The specific method of fixing the sheet of G10 in the surrounding concrete has yet to be finalized. However, the edge conditions for the calculations remain the same regardless of what material or method is used. The $5\text{ m} \times 5\text{ m}$ area of the G10 window matches the dimensions of the cylindrical TPC (5 m diameter, 5 m long) in the gas vessel. This ensures the entire area of the gas TPC would see the low radiation length. The radiation length through the eight layers of the ArgonCube cryostat wall, using G10 instead of concrete, is 0.8. Table 28 summarizes each layer and the corresponding radiation lengths.



Figure 26: Layers of ArgonCube cryostat's low radiation-length thickness wall (layers not to scale)

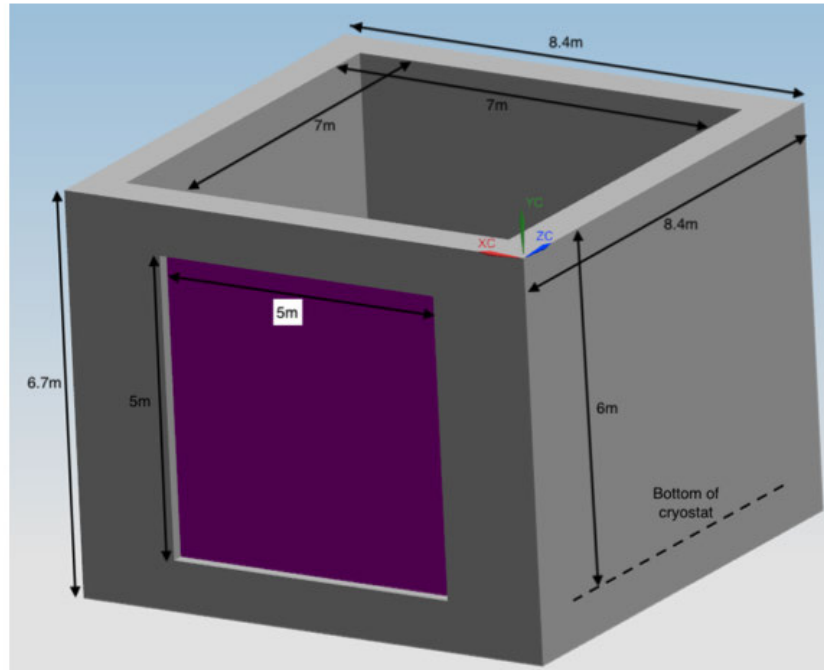


Figure 27: Dimensions of ArgonCube cryostat

Layer	Radiation Length based on Material Composition		Density	Thickness	Calculated Radiation Length	Percentage of Total Radiation Length
	g/cm^2	mm	g/cm^3	mm	unitless	%
304 SS Membrane	13.904	17.6	7.9	2	0.11	14.16
Fireproof Board	23.955	399.25	0.6	10	0.03	3.12
Insulation 1st Layer	40.8	5440	0.075	190	0.03	4.35
Insulation 2nd Layer	40.8	5440	0.075	200	0.04	4.58
Carbon Steel	7.85	17.60	7.9	1.2	0.07	8.50
G10 Sheet	32.98	194	1.7	101.6	0.52	65.28
Total Radiation Length					0.80	100.00

Figure 28: ArgonCube cryostat layers in units of radiation length.

Using the 35 t as a baseline again, it was assumed that the maximum design pressure in the ArgonCube cryostat would be approximately 20.6 kPa (3 psig). That pressure, combined with the hydrostatic pressure of 67.6 kPa (9.8 psig), equals a total pressure of 88.2 kPa (12.8 psig) applied uniformly across the G10 window. A finite element analysis of the pressure on this G10 window is reported in section A.1.5.

G10 was chosen as the material for the window due to its high strength and low thickness in radiation lengths. In addition, sheets of Aluminum and Titanium were tested in place of the G10 window. With these materials, the resulting total wall thickness was $1.16 X_0$ for all layers including Aluminum and $1.96 X_0$ for all layers including Titanium. Below, we also include calculations for a Carbon Fiber window.

A.1.5 FEA Results of G10 Window in ArgonCube Cryostat

Ang Lee (Fermilab) completed a finite element analysis (FEA) to analyze the G10 window and insulation. A total pressure of 88.2 kPa (12.8 psig) was applied to the window and insulation: 67.6 kPa (9.8 psig) of hydrostatic pressure and 20.6 kPa (3 psig) of uniform pressure (see Figure 29). A vertical plane of symmetry was applied to the window for ease of analysis. This is clarified in Figure 30. Four cases were analyzed with different boundary conditions:

1. Case 1a
 - Outer 4 walls of G10 are fixed
 - G10 and insulation are not bonded
2. Case 1b:
 - Outer 4 walls of G10 are fixed
 - G10 and insulation are bonded
3. Case 2a:
 - Outer 4 walls of G10 and insulation are fixed
 - G10 and insulation are not bonded
4. Case 2b:

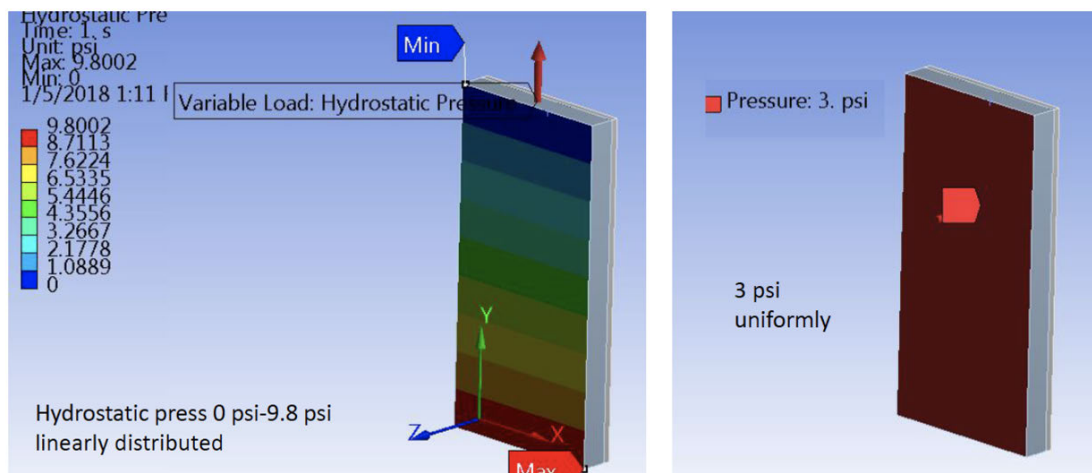


Figure 5: Pressure boundary conditions for G10 window and insulation

Figure 29: Pressure boundary conditions for G10 window and insulation

Half -Symmetry Surface

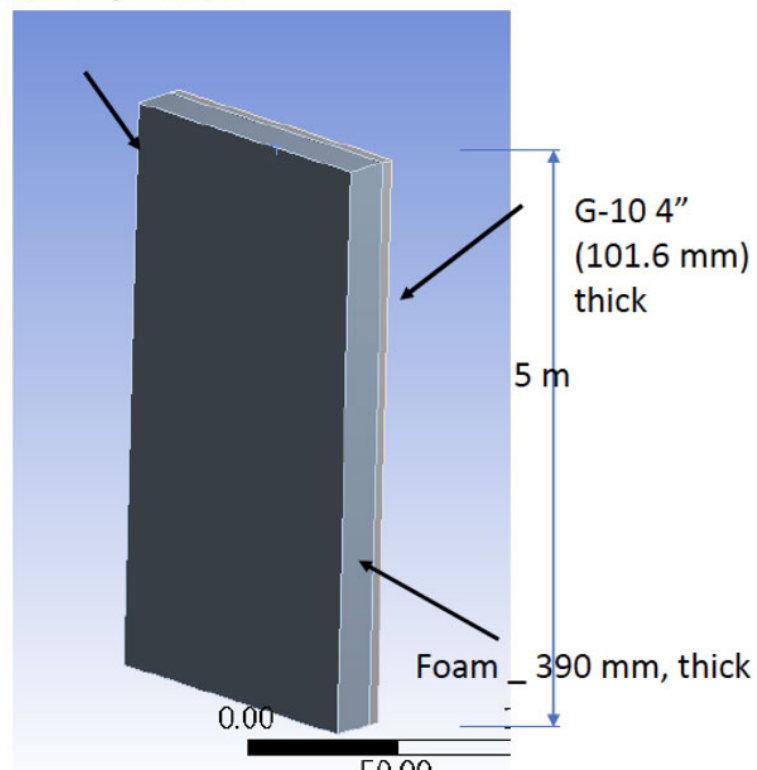


Figure 6: Dimensions of window and plane of symmetry

Figure 30: Vertical symmetry plane.

- Outer 4 walls of G10 and insulation are fixed
- G10 and insulation are bonded

Table 4: Results of FEA on G10 window and insulation

Case	1a	1b	2a	2b
Window deflection (mm)	28.60	21.46	27.25	19.15
Window deflection (inches)	1.126	0.845	1.073	0.754
Stress on G10 (MPa)	40.65	36.59	37.31	30.74
Stress on G10 (psi)	5,896	5,307	5,411	4,458

Figure 31: Results of FEA on G10 window and insulation

The results are located in Figure 31. The worst-case scenario is 1a. Even with these boundary conditions (outer four walls of the G10 are fixed and the G10 and insulation are not bonded), a deflection of 28.6 mm (1.126 in) is minimal compared to the overall size of the window. Additionally, the applied stress of 40.65 MPa (5,896 psi) is well below the tensile and compressive strengths of the G10: 257 MPa (32,278 psi) and 448 MPa (65,000 psi), respectively [23]. The majority of the 88.2 kPa (12.8 psig) pressure applied to the window is absorbed by the G10 window, but the insulation does experience some of the stress. The tensile and compressive strengths of the Rohacell insulation are 100 kPa (145 psi) and 400 kPa (58 psi), respectively [24]. These are larger than the maximum (tensile) and minimum (compressive) principal stresses on the insulation. From the FEA, the maximum principal stress is 148 kPa (21.5 psi) and the minimum principal stress is 153 kPa (22.2 psi). These results are shown in Figure 32. Similarly, the shear stress on the insulation is 100 kPa (14.48 psi) from the FEA results. This is less than the shear strength of Rohacell, 400 kPa (58 psi) [24]. The properties of Rohacell 31A were used for the FEA, however Rohacell 51A and Rohacell 71A have higher strength properties and could be considered in future analyses.

A.1.6 Analysis with Carbon-fiber window for the ArgonCube Cryostat

Another material that could be used for the thin window is carbon fiber. The carbon-fiber window would consist of a layer of insulation sandwiched between two layers of carbon fiber. A maximum deflection of 22mm (0.89in) was determined from an FEA completed by Ang Lee. The layers of a carbon fiber window are listed below in Figure 33. Figure 34 shows the thickness of the layers of the cryostat wall with the carbon fiber window instead of G10. A window of carbon fiber would produce a total radiation length to 0.29 X_0 . This analysis is ongoing.

A.1.7 Conclusions

The proposed design for the ArgonCube cryostat provides a minimized radiation length through the cryostat wall while maintaining structural requirements for a cryostat of this size. With a 0.1 m

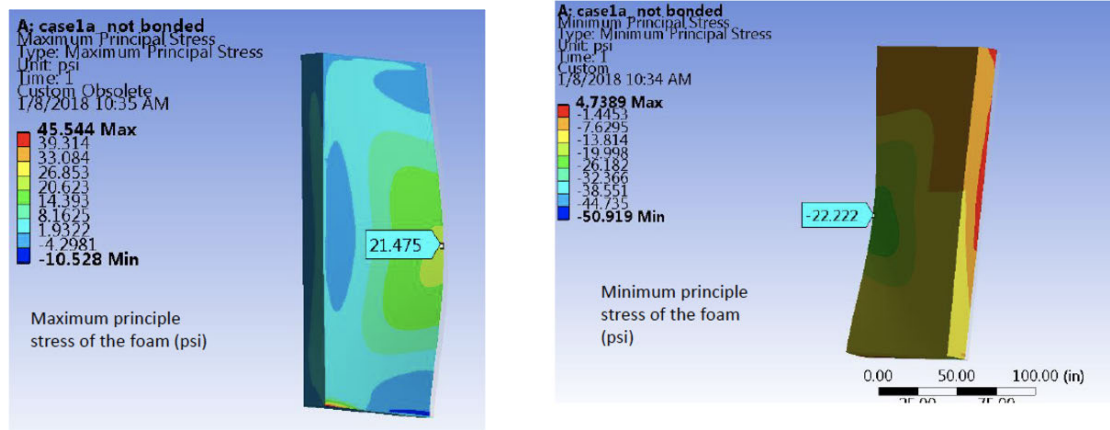


Figure 7: Maximum and minimum principle stresses applied to Rohacell insulation

Figure 32: Maximum and minimum principle stresses applied to Rohacell insulation

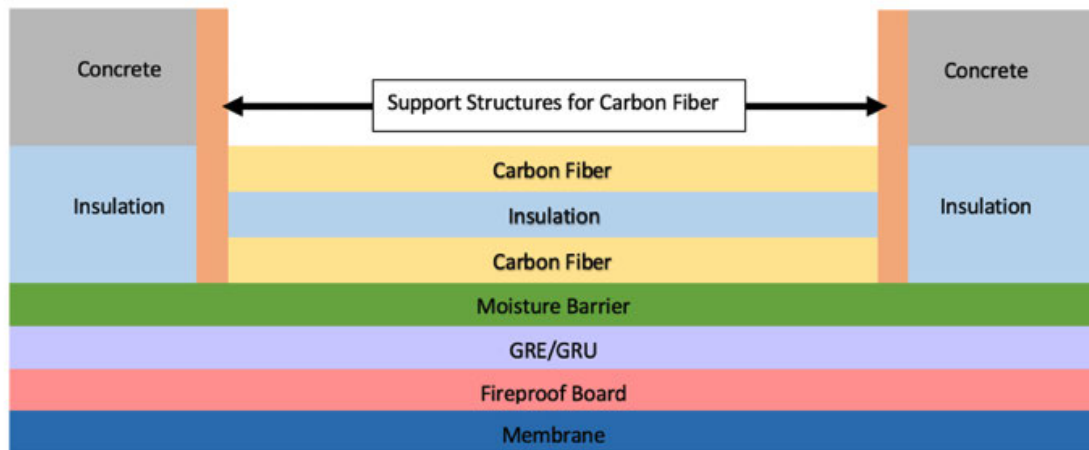


Figure 8: Layers of cryostat wall with carbon fiber window (layers not to scale)

Figure 33: Radiation Lengths of ArgonCube Cryostat with Carbon Fiber

Table 5: Radiation Lengths of ArgonCube Cryostat with Carbon Fiber

ArgonCube Cryostat- Carbon Fiber						
Layer	Radiation Length based on Material Composition		Density	Thickness	Calculated Radiation Length	Percentage of Total Radiation Length
	g/cm ²	mm			unitless	%
304 SS Membrane	13.904	17.6	7.9	2	0.11	39.68
Fireproof Board	23.955	399.25	0.6	10	0.03	8.75
Carbon Steel	7.85	17.60	7.9	1.2	0.07	23.81
Carbon Fiber	52.14	237	2.2	5	0.02	7.37
Insulation	40.8	5440	0.075	203.2	0.04	13.04
Carbon Fiber	52.14	237	2.2	5	0.02	7.37
Total Radiation Length					0.29	100.00

Figure 34: Layers of cryostat wall with carbon fiber window (layers not to scale)

thick G10 window in one of the cryostat walls, the total thickness of the wall is 0.8 radiation lengths. Using carbon fiber instead of G10 reduces this number to 0.29 radiation lengths. The basis for the ArgonCube cryostat stems from the 35T cryostat, which was successfully built at Fermilab in 2014 and has been operational since then.

A.2 Dipole magnet considerations

Initial studies for the construction of an electromagnet similar to the UA1 magnet predict that the cost of the design, procurement, infrastructure (power and cooling) and assembly will be on the order of 20 million USD, before operation costs. The cooling requirement for the comparable UA1 magnet (operating at 0.2 T as part of the ND280 Off-axis Detector [25]) is 450 kW ($I_{\text{nom}}=2900$ A, $V_{\text{nom}}=155$ V). A detailed design study [26] has been done for the electromagnet discussed in section 3, which shows that in order to reach a central field between 0.4 T and 0.45 T, power dissipation in the magnet is ≈ 2.3 MW. Adding in power consumption for the water cooling system brings this number closer to 3 MW. At this power level, the estimated operational cost is about 1.3 M US\$ per year. The infrastructure costs for a 3 MW industrial cooling water (ICW) system are estimated to be in excess of \$3M. These operational and cooling water requirements have to be considered for DUNE over the duration of the experiment. Additionally, the coil structure and its support bobbin puts about 20 radiation lengths of material in the path of the tracks generated in and exiting from the liquid argon TPC, before they reach the outer ECAL section and the FGT.

A superconducting magnet offers advantages by shifting the cooling requirements from ICW to cryogenic gases. The big advantage of a superconducting magnet is the design. Coils can be arranged as a Helmholtz coil, effectively eliminating any material in the beam.

We have performed a preliminary study of a Helmholtz Coil arrangement. Two coils (radius 3.5 m) are separated by 4.8 m. This specification will allow coverage of the active HPgTPC volume and yields an arrangement in which the longitudinal force on the coils is very small (≈ 10 kN). See Figure 35.

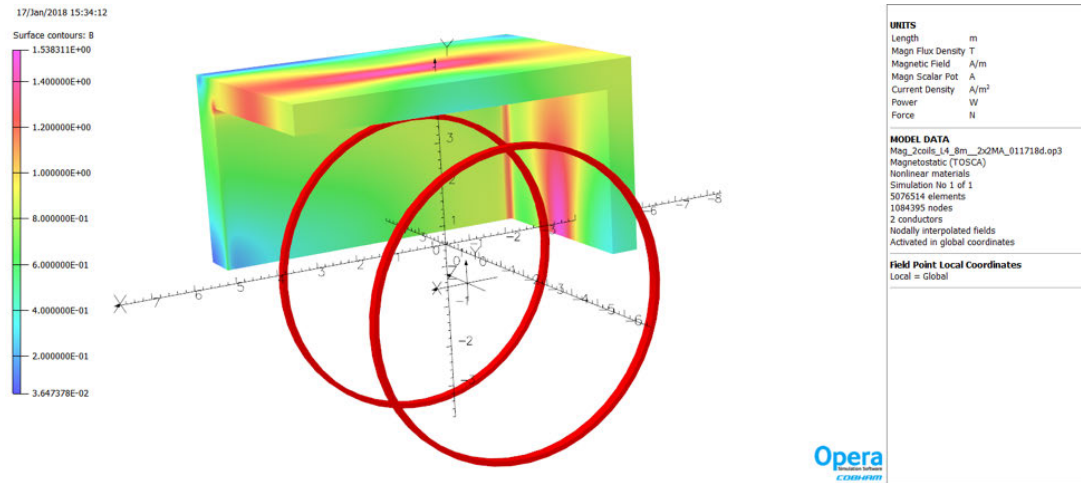


Figure 35: Helmholtz coil arrangement

The field non-uniformity (the B field along the TPC axis for different distances from the TPC center line) is shown in Figure 36. The uniformity increases towards the rotational symmetry

center, as shown in this Figure. Although this non-uniformity is large ($\approx 49\%$), the vertex TPCs in NA49/61/Shine[27] have operated very successfully with their Helmholtz coils, where the field non-uniformity is 60%. Field mapping coupled with analytical calculations (Opera or Tosca) are required, however.

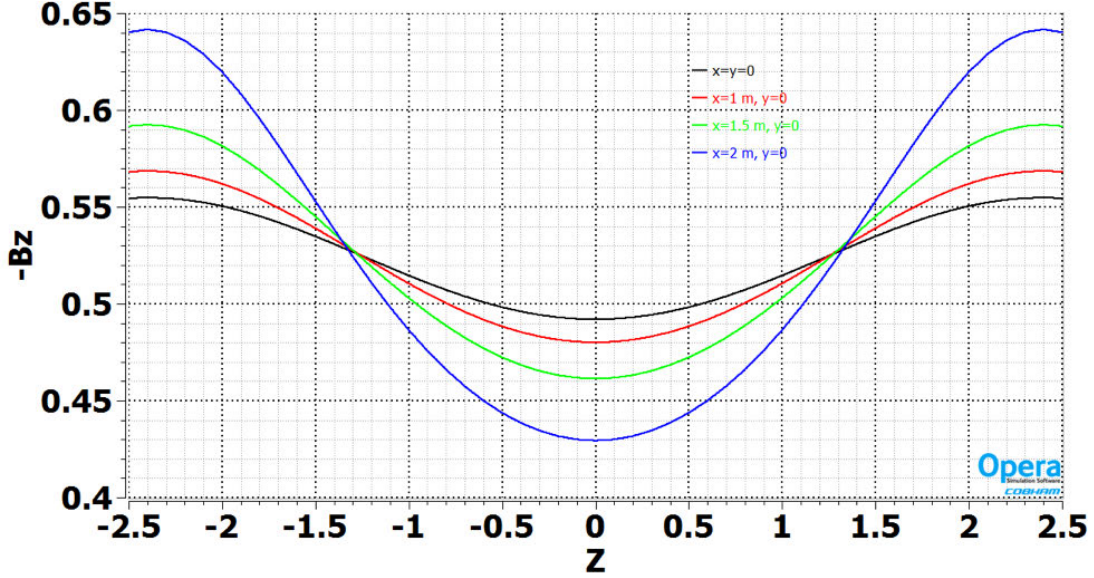


Figure 36: B field along TPC axis (z) as function of distance from TPC center line.

The coil will be constructed from aluminum stabilized niobium titanium (NbTi). The conductor is the same as that used in the $\mu 2e$ detector solenoid[28] (spare conductor is available). The coil pack has a current of 2 MA, the size is 125 mm by 240 mm. Return iron surrounding the TPC (see Figure ??) is open on the side towards ArgonCube to allow particles to pass without additional material. The stored energy is ≈ 80 MJ. A study of the potential use of a trim coil indicated significant improvement of the field uniformity, if so desired. See Figures 37 and Figures 38. In this case the overall field non-uniformity is 16%.

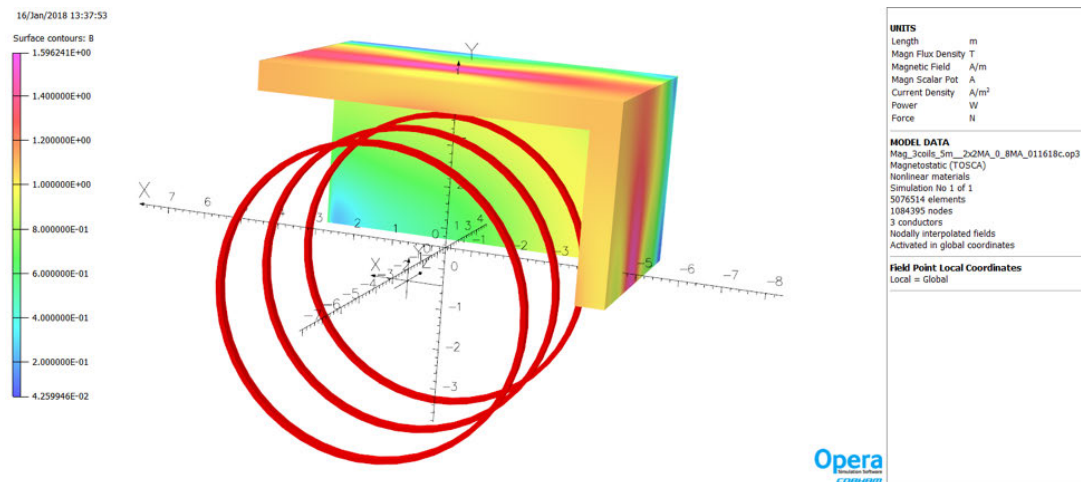


Figure 37: Configuration with main coils with the addition of a central trim coil.

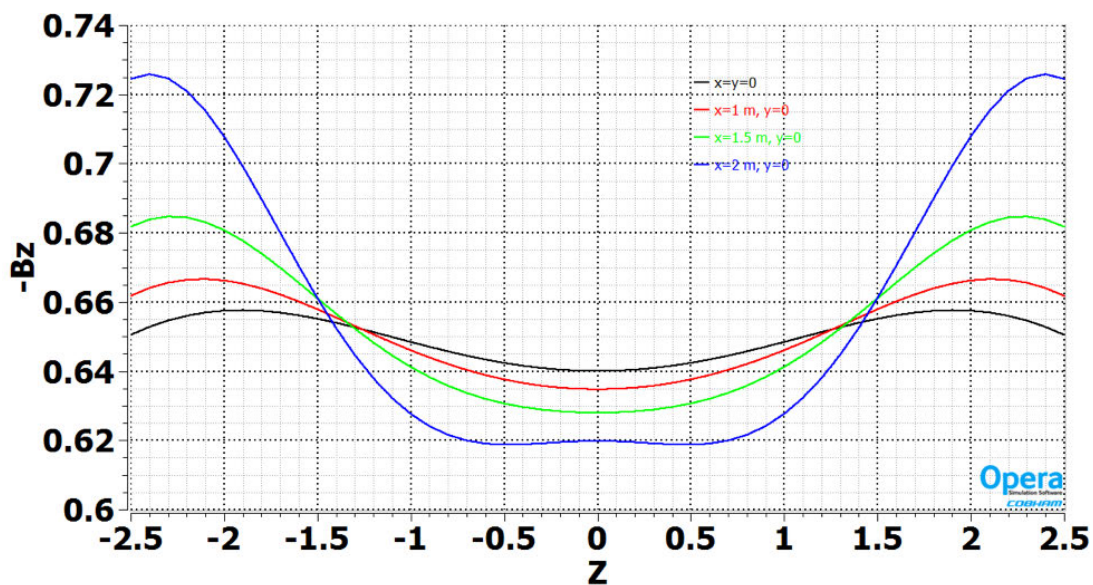


Figure 38: B field along TPC axis (z) as function of distance from TPC center line in 2 coil + trim configuration.

A.3 TPC Pressure vessel design

A preliminary design study for a pressure that allows for the TPC plus part of the ECAL to be inside the gas volume (see section 4.5) is presented in Figure 39. It is fabricated from stainless steel, has a cylindrical section that is 6 m in diameter and 6 m long and utilizes two semi-elliptical end pieces with flanges. The cylindrical section is $\approx 1.6X_0$ in thickness. Reducing this number further can be accomplished with a change in material (Ti) or with the addition of stiffening rings. The vessel is rated for 175 psia. The cost of the flanging is significant, so we will also consider vessel designs with a fully-welded vessel that can be opened without invalidating the pressure-vessel code (as is the case with the MicroBooNE vessel) and a design with one flange. With modern electronics, signals can be brought out on a few optical fibers thus drastically reducing the cable plant which would make routing cables from the far end much simpler. Given the size of the end pieces, a “human” access port could be incorporated into the end piece(s).

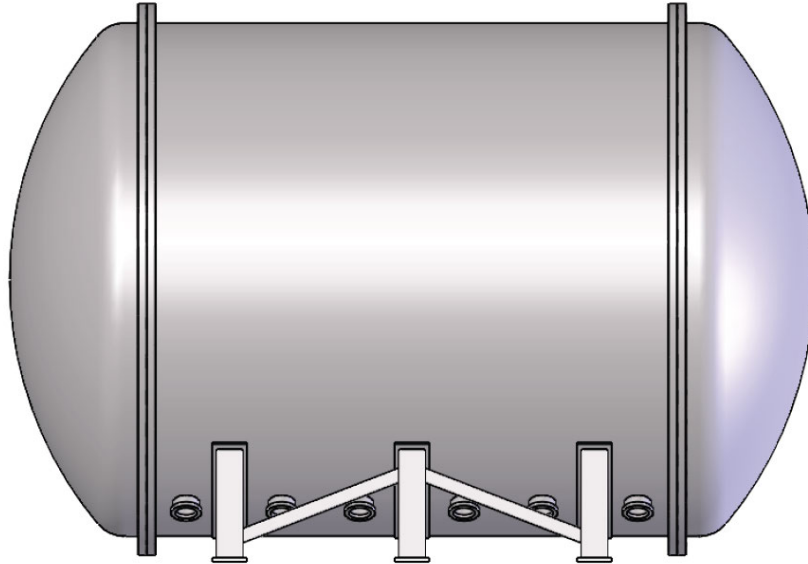


Figure 39: Pressure vessel preliminary design

B HP TPC test Stand

The two main goals of the High Pressure TPC test Stand are to prove that ALICE readout chambers operate stably at a pressure of 10 atm and to provide a platform to test future development related with the technology like different gas mixtures, readout system, field cage technologies, etc. The test stand is located at the Proton Assembly Building (PAB) at Fermilab. It is currently assembled for data taking at 1 atm pressure while the gas system is being upgraded to handle higher pressure. Figure 40 shows a picture of the current setup. The following subsections detail its main components.

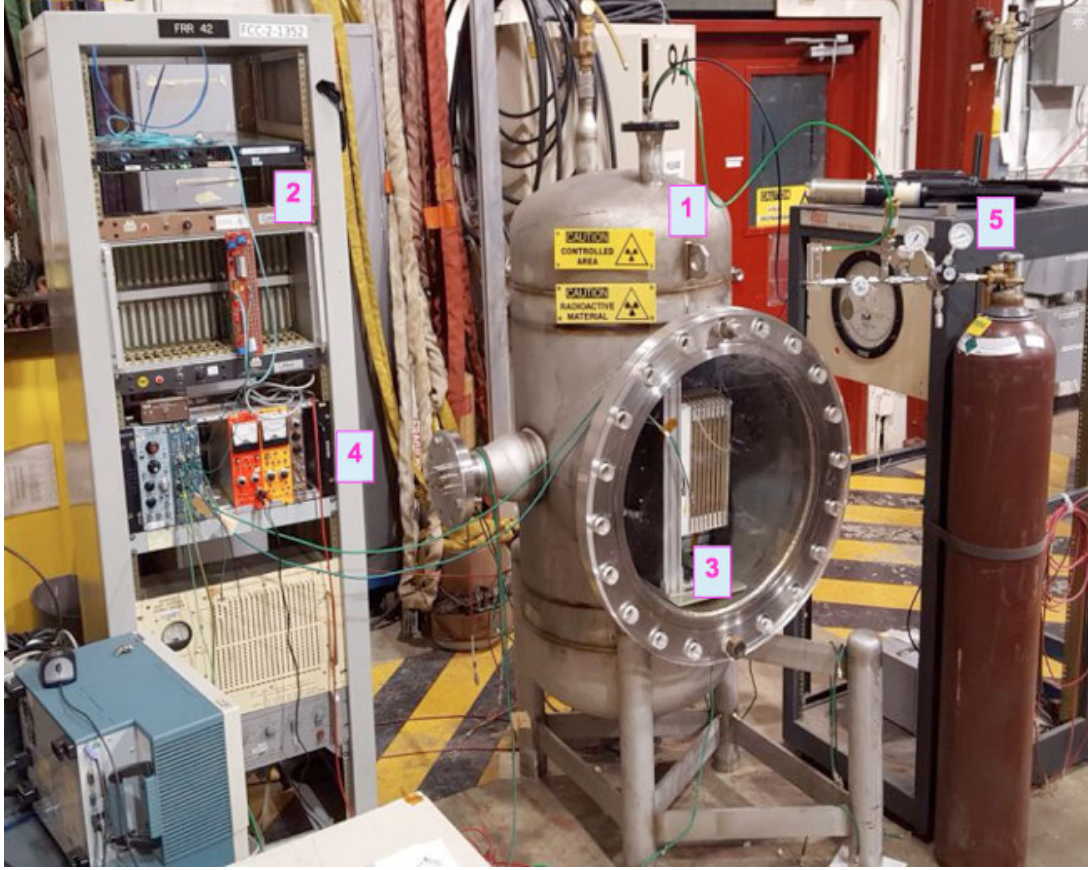


Figure 40: Picture of the test stand at PAB at Fermilab.

B.1 Test vessel

The pressure vessel (element 1 in Fig. 40) is rated for running up to a pressure of 10 atm. It has four access ports to the inner volume: the large front window for detector installation, two small holes on the top for the inlet/outlet piping and vacuum pipe, and one extra access port on the side used for readout and control signals. The vessel is 4 ft tall with a cylindrical cross section with a diameter of 2 ft.

B.2 Readout chamber and field cage

One of the spare inner readout chambers (IROC) of the ALICE detector has been lent to the group for the high-pressure test. Figure 41 shows pictures of the IROC at Fermilab: detector side (a) and connector side of the chamber (b). Its readout plane is divided in 5504 individual pads for true 3D operation. Each pad is 4 mm by 7 mm in size and collects the induced signal from free carriers produced in the multiplication volume. Two wire planes separated 2 and 4 millimeters from the pad plane each provide a high electric field volume between them for signal amplification of the primary ionization electrons. More information is detailed in [29]. Gains ranging from 1 to 10×10^5 have been measured by the ALICE group with voltages between these wire planes below 1350 V. This voltage is expected to be lower at high pressure operation. A third wire plane (gating grid)

located 7 mm away from the pad plane is used to control the access of the primary electrons to the multiplication region.

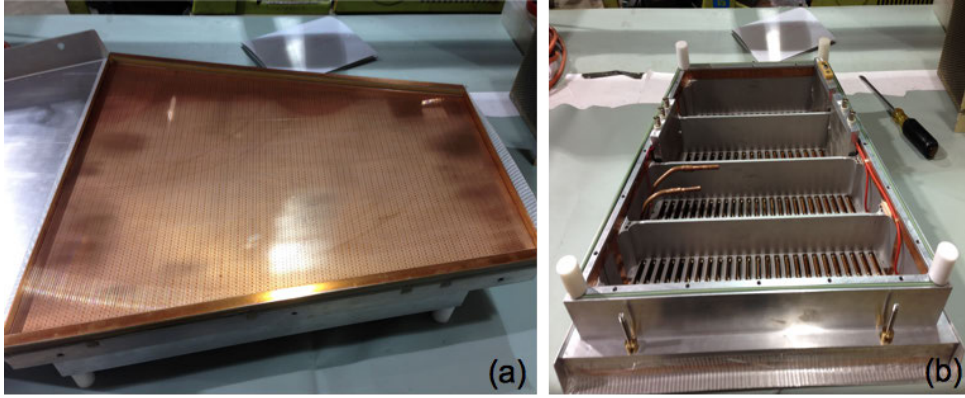


Figure 41: Front and back view of the IROC.

The field cage design conceptually follows ALICE test box field cage with a different sizing to accommodate it together with the IROC inside the pressure vessel. Figure 42(a) shows a picture of the field cage. During detector assembly the field cage is attached to the chamber as one piece and moved together through the big window into the vessel (label 3 in Fig. 40). The field cage active volume is approximately 25 L.

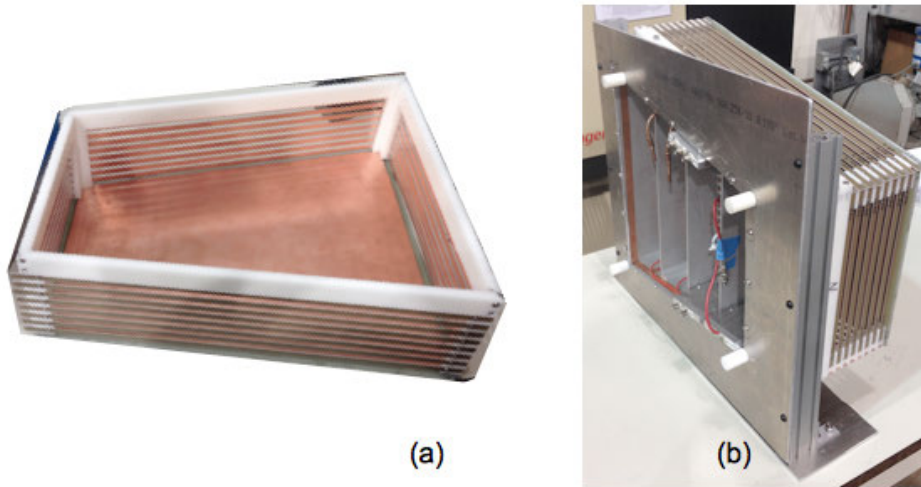


Figure 42: Field cage (a) design for the high pressure stand and how it goes assembled together with the IROC.

B.3 Readout electronics and DAQ system

The data acquisition system and readout electronics have been inherited from liquid argon experiments at Fermilab. Each front-end electronics board has 64 charge amplifiers that collect the induced signals of each pad and send them to the digitizers. These boards have demonstrated good

operation as the cold electronics for the LArIAT experiment [30], and its performance, in terms of signal noise, is not considerably reduced when operating at room temperature, as in the case for the high-pressure test stand. Figure 43 displays its RMS noise in the output signals of the boards as a function of temperature. A new cable has been design and fabricated to adapt the boards to the IROC. Figure 44 shows a sample of the first batch of cables.

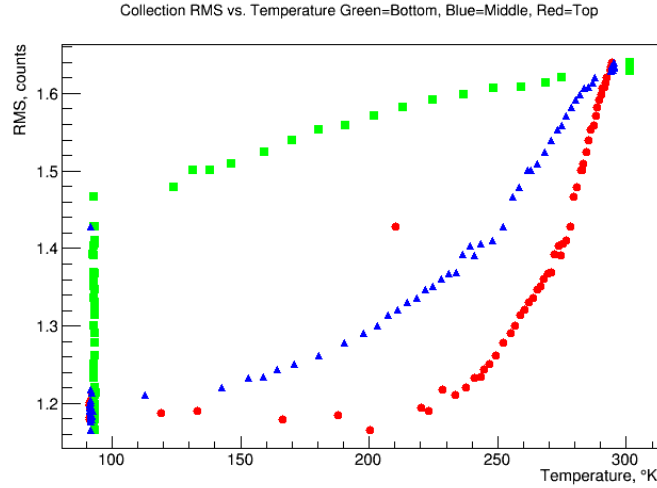


Figure 43: RMS noise of the front-end electronics as a function of the running temperature

The data acquisition system is based on CAEN V1740 digitizers connected through optic fiber to a server that uses the same data acquisition framework as other liquid Argon experiments at Fermilab. These two components are marked with label "2" in Fig. 40. The output data is processed offline using available liquid argon software tools.

Some tests require measurement of DC component of the current taken by the detector. In this case, picoammeters such as the Keithley 485 are used.



Figure 44: New kapton cable for single pad connection to front-end electronics.

B.4 Gas system

The current gas system is designed to be an open loop system. The gas mixture is supplied directly by a gas cylinder as shown in Fig. 40, labeled "5". The current piping supports operation at 1 atm pressure while the high-pressure design is being built. Figure 45 shows the final design for high-pressure operation. It allows steady operation at any pressure up to 10 atm and provides a

vacuum system line to purge the vessel for cleaning and quick start-up time purpose. Some of the components for high pressure operation are being assembled and tested.

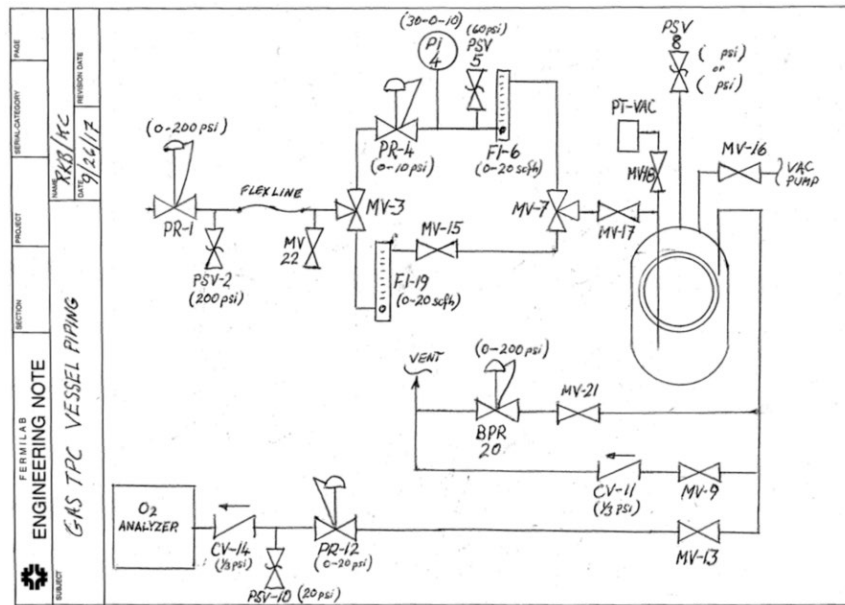


Figure 45: Gas system final design

B.5 Near-future schedule for the test stand

The current schedule for the test bench follows three main steps: validate results from ALICE collaboration, prove steady operation at pressures up to 10 atm, and run the detector for particle identification at high pressure in a test beam. The timeline of these steps is as follows.

- *Validate ALICE results:* Already started and will continue for the next 4 months.
- *Increase operation pressure:* Starting in 2 months.
- *Run at test beam:* Starting in approximately 6 months.

References

- [1] C. W. Fabjan et al. (ALICE), J. Phys. **G32**, 1295 (2006).
- [2] S. Dytman, AIP Conf. Proc. **1680**, 030002 (2015).
- [3] C. Cheshkov (ALICE Collaboration), Nuclear Instruments and Methods in Physics Research Section A: Accelerators, Spectrometers, Detectors and Associated Equipment **566**, 35 (2006), ISSN 0168-9002, tIME 2005, URL <http://www.sciencedirect.com/science/article/pii/S0168900206008059>.
- [4] D. H. Stork (PEP4), J. Phys. Colloq. **43**, 42 (1982).
- [5] J. Boyer et al., Phys. Rev. **D42**, 1350 (1990).
- [6] C. Lippmann, Phys. Procedia **37**, 434 (2012).

- [7] (????), <https://physics.nist.gov/PhysRefData/Star/Text/intro.html>.
- [8] B. B. Abelev et al. (ALICE), *Int. J. Mod. Phys. A* **29**, 1430044 (2014), [1402.4476](#).
- [9] R. Acciarri et al. (DUNE) (2015), [1512.06148](#).
- [10] C. Andreopoulos et al., *Nucl. Instrum. Meth. A* **614**, 87 (2010), [0905.2517](#).
- [11] C. Andreopoulos, C. Barry, S. Dytman, H. Gallagher, T. Golan, R. Hatcher, G. Perdue, and J. Yarba (2015), [1510.05494](#).
- [12] LArSoft Collaboration, *LArSoft*, <http://larsoft.org>, online; accessed 16-Jan-2018.
- [13] C. Adloff et al. (CALICE), *JINST* **5**, P05004 (2010), [1003.2662](#).
- [14] F. Simon and C. Soldner, *Nucl. Instrum. Meth. A* **620**, 196 (2010), [1001.4665](#).
- [15] Y. Liu, V. Büscher, J. Caudron, P. Chau, S. Krause, L. Masetti, U. SchÄdfer, R. Spreckels, S. Tapprogge, and R. Wanke, in *Proceedings, 21st Symposium on Room-Temperature Semiconductor X-ray and Gamma-ray Detectors (RTSD 2014): Seattle, WA, USA, November 8-15, 2014* (2016), p. 7431118, [1512.05900](#), URL <http://inspirehep.net/record/1410633/files/arXiv:1512.05900.pdf>.
- [16] F. Simon, C. Soldner, and L. Weuste, *JINST* **8**, P12001 (2013), [1309.6143](#).
- [17] N. V. Mokhov, in *Proceedings, 6th Meeting on Shielding Aspects of Accelerators, Targets and Irradiation Facilities (SATIF-6): Menlo Park, California, April 10-12, 2002* (2003), URL http://lss.fnal.gov/cgi-bin/find_paper.pl?conf-03-053.
- [18] (????), ALICE software, <https://alisw.github.io/>.
- [19] Peter G. Noble, *A short history of LNG shipping, 1959-2009*, texas Section, SNAME, 2009.
- [20] Wikipedia, *LNG Carrier*, https://en.wikipedia.org/wiki/LNG_carrier, accessed: 15-Dec-2017.
- [21] D. Montanari et al. (LBNE), *AIP Conf. Proc.* **1573**, 1664 (2014).
- [22] T. Tope et al., *AIP Conf. Proc.* **1573**, 1169 (2014).
- [23] Carl L. Goodzeit, *Superconducting Accelerator Magnets, An Introduction for Mechanical Design and Construction*, January, 2001.
- [24] Rohacell composites, *Technical information - Rohacell A*, <http://www.rohacell.com/product/rohacell/en/products-services/rohacell-s/pages/default.aspx>, online; accessed 15-Jan-2018.
- [25] E. Frank, Ph.D. thesis, Bern U. (2012), URL <http://www.t2k.org/docs/thesis/localDocDetail?docid=021>.
- [26] Sanjib Mishra, *Internal Technical Design Review of the DUNE-ND*, May, 2015.
- [27] S. Afanasev et al. (NA49), *Nucl. Instrum. Meth. A* **430**, 210 (1999).
- [28] V. Lombardo, M. Buehler, M. Lamm, T. Page, S. Curreli, P. Fabbriatore, and R. Musenich (Mu2e), *IEEE Trans. Appl. Supercond.* **26**, 4804105 (2016).
- [29] J. Alme, Y. Andres, H. AppelshÄduser, S. Bablok, N. Bialas, R. Bolgen, U. Bonnes, R. Bramm, P. Braun-Munzinger, R. Campagnolo, et al., *Nuclear Instruments and Methods in Physics Research Section A: Accelerators, Spectrometers, Detectors and Associated Equipment* **622**, 316 (2010), ISSN 0168-9002, URL <http://www.sciencedirect.com/science/article/pii/S0168900210008910>.

[30] F. Cavanna, M. Kordosky, J. Raaf, and B. Rebel (LArIAT) (2014), [1406.5560](#).